

A bionic approach for the mechanical and electrical decoupling of an MEMS capacitive sensor in ultralow force measurement

Wendi GAO^{a,b,c,d}, Bian TIAN^{a,b}, Cunlang LIU^a, Yingbiao MI^a, Chen JIA (✉)^{a,b}, Libo ZHAO (✉)^{a,b}, Tao LIU^a, Nan ZHU^a, Ping YANG^{a,b}, Qijing LIN^{a,b}, Zhuangde JIANG^{a,b}, Dong SUN^{a,e}

^a State Key Laboratory for Manufacturing Systems Engineering, International Joint Laboratory for Micro/Nano Manufacturing and Measurement Technologies, Overseas Expertise Introduction Center for Micro/Nano Manufacturing and Nano Measurement Technologies Discipline Innovation, Xi'an Jiaotong University (Yantai) Research Institute for Intelligent Sensing Technology and System, School of Mechanical Engineering, Xi'an Jiaotong University, Xi'an 710049, China

^b Shandong Laboratory of Yantai Advanced Materials and Green Manufacturing, Yantai 265599, China

^c State Key Laboratory of Robotics and Systems (HIT), Harbin 150006, China

^d Beijing Advanced Innovation Center for Intelligent Robots and Systems, Beijing Institute of Technology, Beijing 100081, China

^e Department of Biomedical Engineering, City University of Hong Kong, Hong Kong, China

✉ Corresponding author. E-mails: jiachen0224@stu.xjtu.edu.cn (Chen JIA); libozhao@mail.xjtu.edu.cn (Libo ZHAO)

© Higher Education Press 2023

ABSTRACT Capacitive sensors are efficient tools for biophysical force measurement, which is essential for the exploration of cellular behavior. However, attention has been rarely given on the influences of external mechanical and internal electrical interferences on capacitive sensors. In this work, a bionic swallow structure design norm was developed for mechanical decoupling, and the influences of structural parameters on mechanical behavior were fully analyzed and optimized. A bionic feather comb distribution strategy and a portable readout circuit were proposed for eliminating electrostatic interferences. Electrostatic instability was evaluated, and electrostatic decoupling performance was verified on the basis of a novel measurement method utilizing four complementary comb arrays and application-specific integrated circuit readouts. An electrostatic pulling experiment showed that the bionic swallow structure hardly moved by 0.770 nm, and the measurement error was less than 0.009% for the area-variant sensor and 1.118% for the gap-variant sensor, which can be easily compensated in readouts. The proposed sensor also exhibited high resistance against electrostatic rotation, and the resulting measurement error dropped below 0.751%. The rotation interferences were less than 0.330 nm and $(1.829 \times 10^{-7})^\circ$, which were 35 times smaller than those of the traditional differential one. Based on the proposed bionic decoupling method, the fabricated sensor exhibited overwhelming capacitive sensitivity values of 7.078 and 1.473 pF/ μm for gap-variant and area-variant devices, respectively, which were the highest among the current devices. High immunity to mechanical disturbances was maintained simultaneously, i.e., less than 0.369% and 0.058% of the sensor outputs for the gap-variant and area-variant devices, respectively, indicating its great performance improvements over existing devices and feasibility in ultralow biomedical force measurement.

KEYWORDS micro-electro-mechanical system capacitive sensor, bionics, operation instability, mechanical and electrical decoupling, biomedical force measurement

1 Introduction

The exploration and modulation of cellular physiology and functional mechanisms, such as metabolism [1], cell motility [2], and gene expression [3], have recently drawn considerable attention. Current studies showed that

intracellular behavior is greatly affected by the properties of intracellular organelles and components, wherein force information is measured for characterizing cellular morphology [4] and biophysical properties, such as Young's modulus [5], stiffness [6], and viscosity [7]. Precise force measurement also provides interaction regulation between microtools and targeted cells for minimally invasive micromanipulation, such as cloning

[8], drug delivery [9], and gene editing [10]. Benefiting from easy mass production and integration with robotic end effectors [11], numerous micro-electro-mechanical system (MEMS) sensors on the basis of piezoresistors [12,13], piezoelectric membranes [14,15], optical detectors [16,17], and field-effect transistors [18,19] have been proposed. Compared with the aforementioned counterparts, the capacitive sensor has the following advantages: high sensitivity derived from comb-structured capacitive electrode plates [20]; direct integration with application-specific integrated circuit (ASIC) readouts for portable measurement [21]; operation without the stress concentration of movable structures requiring extreme geometry dimensions in piezoresistive and piezoelectric devices, without fabrication difficulties and with relatively low costs [22]. Substantial effort has been devoted to improve the sensitivity and resolution of capacitive sensors to detect ultralow force signals with strong background noise from the biological environment. Specifically, utilizing the flexible supporting flexures of movable structures can directly decrease the deformation stiffness and increase the sensitivity of the sensor. An area-variant capacitive sensor supported by three asymmetric buckling anti-springs was proposed and had an improved force sensitivity of 27.29 aF/nN, but this nonlinear buckling behavior only exists within a small measurement range of 0.97 μN [23]. Narrowing the air gap between comb plates is preferred for enhancing capacitive output and sensitivity. A gap-variant capacitive sensor with a 0.9 μm air spacing was proposed [24]; its capacitive sensitivity increased to 2.58 fF/nm, but its measurement range and linearity deteriorated as the air gap decreased. Numerous parallel-connected combs within one chip unit have been incorporated in previous practices. However, fabrication deviation and chip size increased as the number of combs increased, and therapy resulted in geometric inconsistency and reduced measurement accuracy. Our group previously reported a bionic capacitive sensor containing multiple internal comb arrays, which had a compact chip size and consistent comb geometry using a three-mask fabrication process. These sensors had high force sensitivity values of 528.76 and 98.54 aF/nN with resolutions of 0.44 and 0.98 nN for gap-variant [25] and area-variant devices [26], respectively. The biological medium and intracellular environment are complex [27,28]; hence, the efficient loading along the sensing axis is normally accompanied with surrounding mechanical interferences, which can push movable combs and change their relative position between paired fixed comb plates, and such coupling loadings produce huge disturbances on the sensor output [29]. For the typical laterally movable structure in the aforementioned works [23–26], the planar crosstalk can be largely eliminated by adopting supporting beams with large stretch stiffness. However, a strong mechanical coupling from the vertical loadings

exists. Traditionally, a thick supporting beam is adopted to enhance the vertical bending stiffness. A gap-variant capacitive sensor with straight beams of 50 μm thickness has been developed, and its coupling output from vertical loadings reached 3.226% of the same lateral loading [30]. Folded springs with an increased thickness of 75 μm were utilized, and an area-variant capacitive sensor with an improved selectivity of 1.926% was developed [31]. However, the increased thickness inevitably reduced the structure compliance along the sensing direction. The deformation sensitivity was less than 0.933 fF/ μm for the device [30] and 0.595 pF/ μm for the device [31]. To solve this trade-off problem, a novel mechanical decoupling approach was proposed. Compared with previous works, the crosstalk coupling disturbances were further eliminated by the optimization of a bionic swallow geometry, and a much higher sensitivity and linearity were simultaneously obtained in this work.

Capacitive response is measured with a subjected voltage bias across comb pairs, and parasitic electrostatic force pulls the movable combs toward the fixed one [32]. Previous practices adopted differential combs to generate opposite electrostatic forces [33], which are unsuitable for gap-variant devices, because the generated electrostatic forces increase nonlinearly as a function of the remaining air gap. Once the electrostatic force exceeds a certain amplitude, the pull-in phenomenon, where the movable and fixed comb plates are stuck, occurs [34]. On the basis of the electrostatic stiffness softening effect, pull-in voltage was measured as a reflection of mechanical loads [35], which had an efficient sensitivity of 44.27 $\mu\text{V/nN}$ but with strong nonlinearity. In addition, a nulling mechanism, in which additional comb actuators drive the deformed movable combs back to the desired working position, was introduced [36]. This mechanism had a highly efficient sensitivity of 2.34 mV/nN but only worked for a small-ranged force measurement under 230 nN. Except for the high requirement of precise parameter estimation [37] and complicated control circuits [38], the actuation force of the closed-loop sensing schemes can probably produce uncontrollable damage to fragile biological samples, and its position adjustment process may break the stable contact between the sensor probe and targets, leading to an unnecessary slippery movement. Electrostatic moments derived from differential combs can generate coupling rotation movement, which results in operation instability but is usually neglected in the aforementioned studies. However, rare attention has been paid to these electrostatic interferences in current studies. In this work, a bionic electrostatic decoupling approach was proposed for improving the capacitive sensor stability of MEMS. For comparison with our previously reported work [25,26], two new gap-variant and area-variant type capacitive sensors with four complementary comb arrays were proposed and fabricated. On the basis of these

complementary comb arrays and portable ASIC readouts, the electrostatic instability was comprehensively analyzed, and the effectiveness of the underlying mechanism of the proposed method was verified.

The main contributions of this work are summarized as follows: First, a bionic swallow structure design norm was developed for mechanical decoupling. The influences of structural parameters on the mechanical behavior were fully analyzed and optimized with the proposed mechanical model and simulation. Second, operation instability resulting from electrostatic pulling and rotation was studied for gap-variant and area-variant devices. A bionic feather comb distribution strategy and a portable sensing circuit were proposed to eliminate electrostatic interferences. Third, a novel measurement method utilizing the four complementary comb arrays and ASIC readouts was proposed to evaluate electrostatic instability and verifying the electrostatic decoupling performance, and the proposed approach was compared with traditional differential combs. The bionic swallow structure hardly moved by 0.770 nm for the electrostatic pulling of the area-variant sensor, and the original measurement error was less than 0.009% for the area-variant sensor and 1.118% for the gap-variant sensor, which can be easily compensated in readouts. The proposed sensor also exhibited high resistance against electrostatic rotation, and the measurement error was less than 0.751%. The rotation interferences were less than 0.330 nm and $(1.829 \times 10^{-7})^\circ$, which were 35 times smaller than those of the traditional differential one. Fourth, mechanical decoupling experiments were conducted by utilizing the built robotic microscopy system. The fabricated sensor showed high capacitive sensitivity values of 7.078 and 1.473 pF/ μm for gap-variant and area-variant devices, respectively. High immunity to mechanical disturbances was maintained simultaneously, taking less than 0.369%

and 0.058% of the sensor outputs of the gap-variant and area-variant devices, respectively.

The rest of this article is organized as follows. Section 2 introduces the proposed bionic swallow structure design norm and structural optimization. Section 3 illustrates the analysis of operation instability under electrostatic pulling and rotation, and a bionic feather comb distribution strategy and a portable ASIC readout were introduced in this section. Section 4 presents the fabrication and calibration of the proposed sensor, followed by the mechanical and electrostatic decoupling experiments in Section 5. Lastly, Section 6 draws the conclusions of this study.

2 Mechanical decoupling approach

2.1 Bionic structure design

Through evolving morphological adaptations to air turbulence available in moving winds, swallows can maintain high aerodynamic stability by the soaring–gliding gesture, which is strongly comparable to the interferences of ultralow force measurement in a biomedical environment. Inspired by this novel but rarely noticed observation, a bionic swallow structure is proposed for capacitive sensors, as shown in Fig. 1. Similar to the gliding swallow, two folded wings are placed around the central body region with a tail end. The sensing structure is floated in the air by the straight beams, wherein four beams are located in the corner of the wing region, and the resting two are mounted in the tail region. The proposed sensing structure possesses a beak in the front of the head region, where external loads are applied. Specifically, the force along the sensing axis y can push the swallow body and wing region laterally.

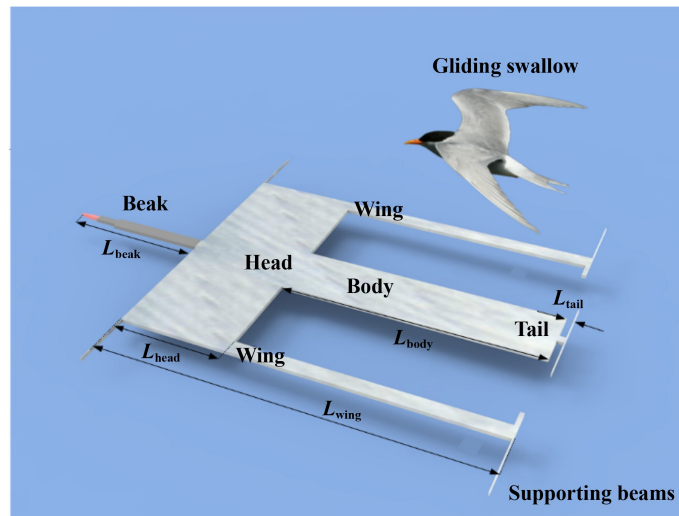


Fig. 1 Schematic of the bionic swallow structure.

The feather-shaped movable combs are integrated along the swallow frame, constituting parallel capacitors with the surrounding fixed combs $C = \frac{\varepsilon L_{co} T_c}{d}$, where ε is the dielectric permittivity in air, and d , L_{co} , and T_c are the gap, overlapped length, and thickness of the comb pair, respectively. During lateral movement, the air gap d changes for the gap-variant type device, and the overlapped length L_c changes for the gap-variant type device. When forces along the x and z axes are applied to the sensor probe, the structure can also be involved in vertical bending or planar rotation, changing the effective L_{co} , T_c , and d , and producing unneglectable interferences on capacitive output. Such mechanical coupling of the proposed swallow structure remarkably relies on geometry parameters, which were modeled and optimized in the subsequent discussion.

2.2 Mechanical modeling and structural optimization

2.2.1 Mechanical behavior under loadings along sensing axis

Forces along three axes were individually applied to the sensor probe to analyze the mechanical behavior of the proposed swallow structure, as shown in Fig. 2. The sensing structure geometry was optimized in terms of its coupling deformation. For the force along the y axis F_y shown in Fig. 2(a), the supporting beams were bent laterally under the reaction forces along the y axis F_{0y1} , F_{0y2} , F_{0y3} , F_{0y4} , F_{0y5} , and F_{0y6} and the moments around the y axis M_{0y1} , M_{0y2} , M_{0y3} , M_{0y4} , M_{0y5} , and M_{0y6} at six fixed ends, and the bending deformation w_y and angle δ_y can be rewritten in terms of F_{0y} and M_{0y} as

$$w_y = \frac{M_{0y1} L_b^2}{2EI_y} - \frac{F_{0y1} L_b^3}{6EI_y}, \quad (1)$$

$$\delta_y = \frac{M_{0y1} L_b}{EI_y} - \frac{F_{0y1} L_b^2}{2EI_y}, \quad (2)$$

where E is the Young's modulus of the structure material, $I_y = \frac{W_b^3 T_b}{12}$ is the moment inertia around the y axis of the beam lateral section, W_b , T_b , and L_b are the beam width, thickness, and length of the supporting beams, respectively.

The swallow structure is considered a rigid body along the y axis because of its larger stiffness compared with that of the supporting beams. As a result, the six supporting beams share identical reaction forces and bending deformation but with zero bending angle δ_y . Substituting $\delta_y = 0$ into Eqs. (1) and (2) yields $M_{0y1} = \frac{F_{0y1} L_b^2}{2EI_y}$ and $w_y = \frac{F_{0y1} L_b^2}{12EI_y}$, respectively. The sum of all forces along the y axis equates to zero, and the reaction force F_{0y1} equals $\frac{F_y}{6}$ for supporting beams at the wing and tail regions. The lateral translation of the swallow structure is solely dependent on the beam size and is illustrated as

$$w_y = \frac{F_y L_b^3}{72EI_y}. \quad (3)$$

To obtain high flexibility along the sensing direction, a narrow width, thin thickness, and long length are much preferable for the supporting beams.

The sensing structure was geometrically modeled with supporting beams of different sizes and simulated with finite element analysis software, ANSYS, to verify the theoretical analysis. Table 1 illustrates the adopted geometry parameters of the swallow structure. In consideration of the achievable fabrication accuracy, W_b and T_b were fixed at 5 and 50 μm , respectively, and L_b was changed from 200 to 800 μm . Figure 3 illustrates the structure deformation under 1 μN force along the y axis, which was sampled along the outside frame of the wing region. Consistent with the theoretical analysis, the supporting beams exhibited the same bending behavior,

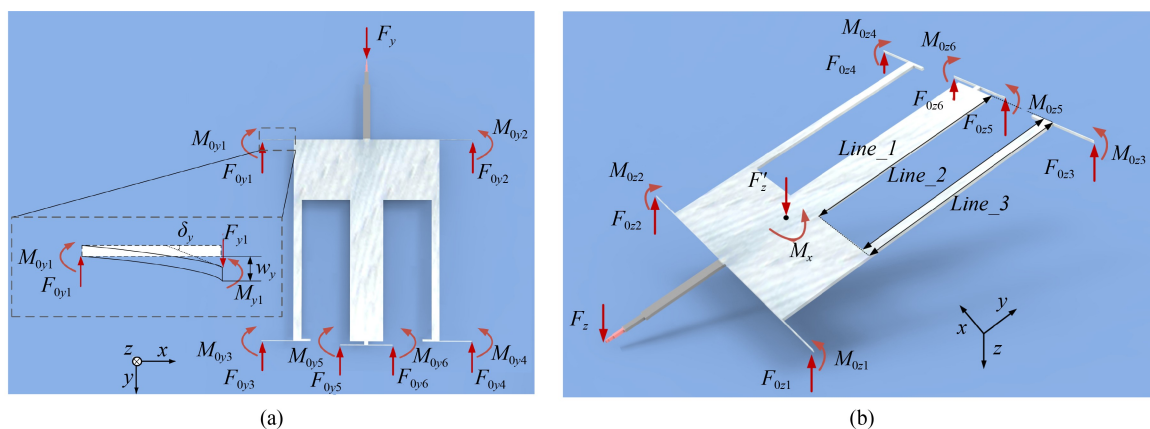


Fig. 2 Schematic of the swallow structure under mechanical forces: (a) swallow structure under lateral force F_y and (b) swallow structure under vertical force F_z .

and the swallow structure implemented a pure translation movement, which presented a cubic increment from 1.625 to 104.270 nm for L_b ranging from 200 to 800 μm . The beam length L_b was therefore set as 600 μm for the balance between low stiffness and fabrication integrity, and the coupling deformation values along the x and z axes were less than 0.018 and 0.003 nm, respectively, which were negligible in comparison with its lateral deformation of 43.939 nm.

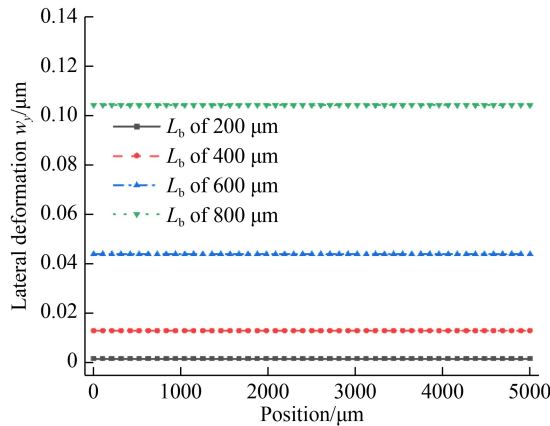
2.2.2 Mechanical behavior under off-axis loadings

When the vertical force F_z was applied to the sensor probe, the swallow structure was deflected under a combination of an equivalent force F'_z and the moment around x axis $M_x = F'_z(L_{\text{beak}} + L_{\text{off}})$, where L_{beak} is the beak probe length and L_{off} is the offset distance between the structure center and front frame of the head region, as shown in Fig. 2(b). Similarly, F'_z pushed the swallow

Table 1 Geometric parameters of the proposed swallow structure

Parameters	Value
Length of the supporting beams, L_b	600 μm
Width of the supporting beams, W_b	5 μm
Thickness of the supporting beams, T_b	50 μm
Length of the beak probe, L_{beak}	2000 μm
Length of the swallow head region, L_{head}	1500 μm
Length of the swallow wing region, L_{wing}	5000 μm
Length of the swallow body region, L_{body}	3500 μm
Air gap of the tri-plate combs, d_{g1}, d_{g2}	3 $\mu\text{m}, 15 \mu\text{m}$
Air gap of the area-variant combs, d_{a0}	3 μm
Overlapped length of the combs, L_{co}	375 $\mu\text{m}^{\text{a)}, 10 \mu\text{m}^{\text{b)}}$
Thickness of the combs, T_c	50 μm

Notes. ^{a)} is for the gap-variant sensor; ^{b)} is for the area-variant sensor.



(a)

structure downward with a translation deformation w_{F_z} of $\frac{F'_z L_b^3}{72EI_z}$, where $I_z = \frac{W_b T_b^3}{12}$ is the moment inertia of the beam vertical section. As for the moment M_x , the swallow structure subjected to the reaction forces along the z axis ($F_{0z1}, F_{0z2}, F_{0z3}, F_{0z4}, F_{0z5}$, and F_{0z6}) and moments around the z axis ($M_{0z1}, M_{0z2}, M_{0z3}, M_{0z4}, M_{0z5}$, and M_{0z6}) is rotated around the x axis. The sum of all moments around the x axis at the structure center is equal to zero and can be expressed as

$$-F_{0z1}D_1 - F_{0z2}D_1 + F_{0z3}D_2 + F_{0z4}D_2 + F_{0z5}D_3 + F_{0z6}D_3 = M_x, \quad (4)$$

where $D_1 = L_{\text{off}} - \frac{W_b}{2}$, $D_2 = L_{\text{wing}} - L_{\text{off}} - \frac{W_b}{2}$, and $D_3 = L_{\text{wing}} + L_{\text{tail}} - L_{\text{off}} - \frac{W_b}{2}$ are the distances between the supporting beam and the structure center, respectively, L_{head} , L_{wing} , and L_{tail} are the lengths of the swallow head, wing, and tail regions, respectively. We first assumed the swallow structure as a rigid body; thus, the bending angle at the joint end δ_z was zero for all beams. The rotation bending deformation of beams w_{M_x} from M_x follows the relationships, $w_{M_{x1}} = w_{M_{x2}}$, $w_{M_{x3}} = w_{M_{x4}}$, and $w_{M_{x5}} = w_{M_{x6}}$, because of the geometric symmetry. Equation (4) can be rewritten as follows in terms of bending deflection:

$$\frac{12EI_z}{L_b^3}D_1w_{M_{x1}} - \frac{12EI_z}{L_b^3}D_2w_{M_{x2}} - \frac{12EI_z}{L_b^3}D_3w_{M_{x3}} = \frac{M_x}{2}. \quad (5)$$

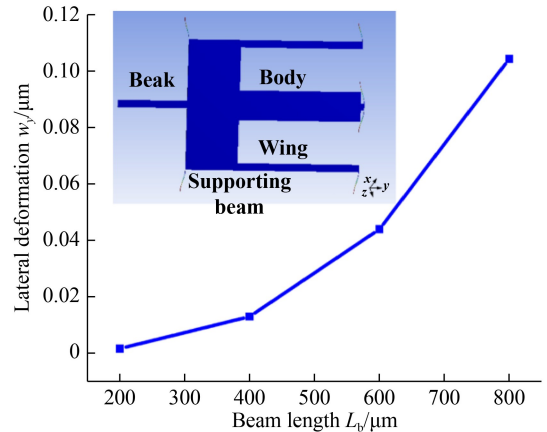
The bending deflection of each beam is proportional to its distance from the center and is expressed as

$$\frac{w_{M_{x1}}}{D_1} = \frac{w_{M_{x2}}}{D_2} = \frac{w_{M_{x3}}}{D_3}. \quad (6)$$

Substituting Eq. (6) into Eq. (5) yields

$$w_{M_{x1}} = \frac{L_b^3 D_1 M_x}{24EI_z (D_1^2 + D_2^2 + D_3^2)}. \quad (7)$$

The swallow structure is easily involved in elastic



(b)

Fig. 3 Simulated vertical deformation w_y under 1 μN of lateral force F_y : (a) w_y of the line along the outside frame of the wing region under different beam length L_b and (b) relationship between w_y and beam length L_b .

deformation $w_E(x, y)$ because of the large planar dimension, which is a function of the tested planar position (x, y) . Thus, the total deformation under F_z should be the sum of w_{F_z} , w_{M_x} , and w_E . The bending deformation along the z axis w_{z1} and w_{z3} can be expressed as

$$w_{z1} = \frac{F_z L_b^3}{72EI_z} + \frac{L_b^3 D_1 M_x}{24EI_z (D_1^2 + D_2^2 + D_3^2)} + w_E(x_1, y_1), \quad (8)$$

$$w_{z3} = \frac{F_z L_b^3}{72EI_z} - \frac{L_b^3 D_1 M_x}{24EI_z (D_1^2 + D_2^2 + D_3^2)} + w_E(x_3, y_3), \quad (9)$$

where (x_1, y_1) and (x_3, y_3) are the joint point positions of the two neighboring supporting beams at the wing region. For F_z with a certain amplitude, the vertical deformation is dependent on the equivalent moment M_x and the planar dimension of swallow structure, among which L_{beak} , L_{head} , and L_{body} play dominant roles.

The sensing structure was modeled and simulated with different beak lengths ranging from 100 to 3000 μm , and the resting geometry parameters were the same as those in Table 1. Figure 4 shows the simulated relationship between L_{beak} and the vertical deformation of the wing outside the frame from point (x_1, y_1) to (x_3, y_3) under an F_z of 1 μN . For a short L_{beak} less than 500 μm , the deformation exhibited a straight-line profile as the swallow wing was rotated around the x axis with small elastic deflection. When L_{beak} exceeded 1000 μm , the swallow wing was bent vertically such that the deformation dropped below zero and a curved transition appeared at points in the wing end, which can compensate for the positive deformation in the beginning, as shown in Fig. 4(a). Positive and negative vertical deformation can change the overlapped area of the comb attached to the swallow structure. The average deformation decreased from 0.784 nm for $L_{\text{beak}} = 100 \mu\text{m}$ to its lowest value of 0.491 nm for $L_{\text{beak}} = 1000 \mu\text{m}$ and then started to increase as L_{beak} increased, as shown in Fig. 4(b). However, the

sensor with a large L_{beak} is favorable because its sensing combs can be conveniently installed outside the narrow space in biomedical applications. L_{beak} was set as 2000 μm in this design, and the average w_z was 0.715 nm, which was comparable with that under a small L_{beak} of 100 μm .

The influences of L_{head} and L_{body} were then simulated using an L_{beak} of 2000 μm . Figure 5(a) illustrates the vertical deformation behavior along the three sampled lines under an L_{head} of 1500 μm . *Line_1* along the swallow body exhibited a smaller peak-to-peak vertical deformation in comparison with *Line_2* and *Line_3* along the inside and outside frames of the swallow wing, respectively. The peak vertical deformation of the three sampled lines decreased as L_{head} increased, indicating that the elastic deformation w_E of the wing and body region became moderate. The average deformation w_z along *Line_2* and *Line_3* rarely changed throughout the L_{head} range, whereas that of *Line_1* decreased rapidly for L_{head} below 1500 μm and became steady afterward, as shown in Fig. 5(b). Thus, L_{head} was set as 1500 μm to integrate more number capacitive combs along the three sampled lines in the swallow wing and body region. The average vertical deformation of *Line_1*, *Line_2*, and *Line_3* were 0.366, 0.242, and 0.243 nm, which were less than 0.71% of the lateral deformation w_y . Compared with the comb thickness T_c of 50 μm , the vertical coupling interferences on capacitor C is ignorable.

Given the high resistance against the suppression or stretch of the straight supporting beams, the structure was rarely deformed under the force along x axis F_x . The maximum deformation along x axis w_x was 0.016 nm for an F_x of 1 μN , whereas the coupling deformation values along the y and z axes were less than 0.015 nm and 0.040 pm, respectively. In other words, the effective comb geometry and the capacitor C remains constant under F_x . The small coupling deformation can be further

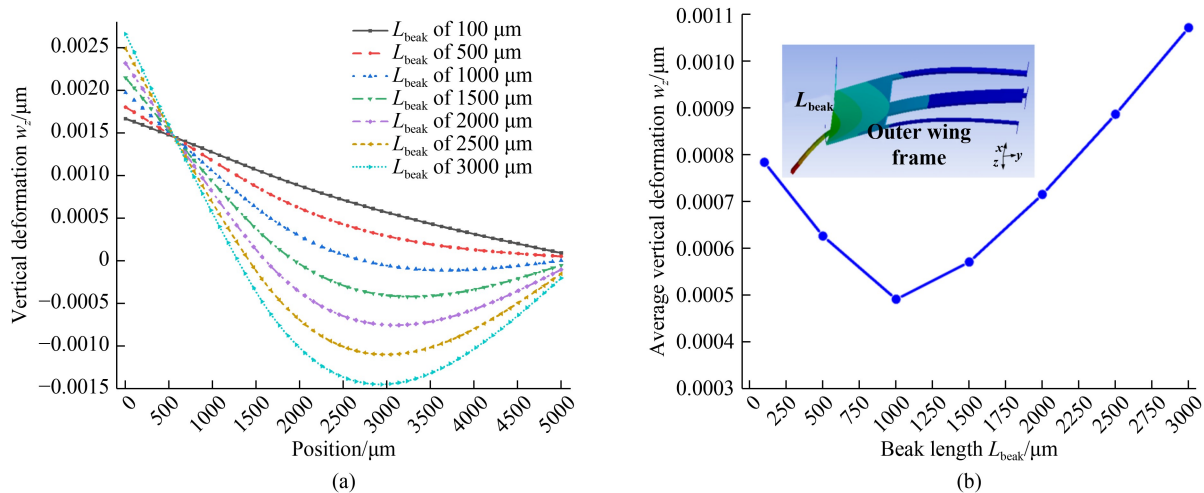


Fig. 4 Simulated vertical deformation w_z along the outer wing frame under different beak length L_{beak} for 1 μN vertical force F_z : (a) w_z of the line along the outside frame of the wing region and (b) calculated average w_z for different beak lengths L_{beak} .

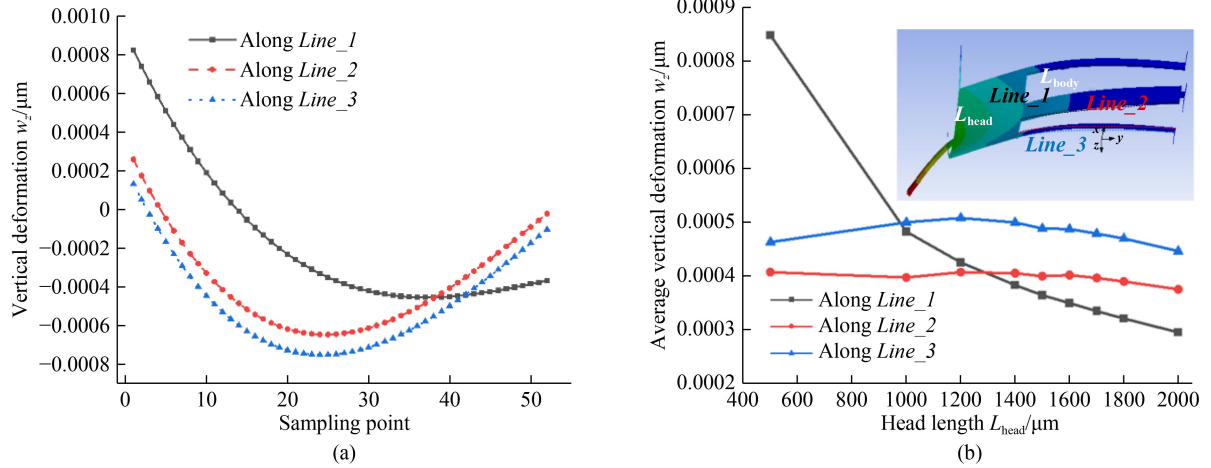


Fig. 5 Simulated vertical deformation w_z for $1 \mu\text{N}$ vertical force F_z : (a) w_z of the three sample lines along the swallow body and wing frame under an L_{head} of $1500 \mu\text{m}$ and (b) calculated average w_z for different head lengths L_{head} .

eliminated through differential sensing output for capacitive sensors. Meanwhile, the proposed structure exhibited high compliance along the sensing direction. Compared with the existing devices, the decoupling performance of the proposed structure was further enhanced, and its force sensitivity was overwhelming, which will be discussed in the subsequent experiments.

3 Electrostatic decoupling approach

3.1 Electrostatic pulling

In this work, the differential and tri-plate configurations were utilized for area-variant and gap-variant devices, as shown in Fig. 6. Even though the generated electrostatic force along the x axis can hardly move the swallow structure, the movable comb can be pulled toward the fixed one by the force along the y axis. For the area-variant devices, the pulling electrostatic force F_{ea} is tangential to the comb plate and is expressed as

$$F_{\text{ea}} = N_a \frac{\varepsilon T_c}{2d_{a0}} V_a^2, \quad (10)$$

where N_a is the number of area-variant combs, and V_a is

the applied voltage bias between the comb plates. With the geometric misalignment derived from fabrication errors neglected, the tangential electrostatic forces in the differential comb pair are equivalent but with opposite charges during structure movement, and electrostatic pulling can be completely canceled out in area-variant combs.

For the gap-variant combs with tri-plate configuration, the movable plate lies asymmetrically in the middle of the two neighboring fixed plates. The efficient normal electrostatic force F_{eg} is a function of the comb position and is expressed as

$$F_{\text{eg}} = N_g \left[\frac{\varepsilon L_{\text{co}} T_c}{2(d_{g1} - y_0 - w_y)^2} V_a^2 - \frac{\varepsilon L_{\text{co}} T_c}{2(d_{g2} + y_0 + w_y)^2} V_a^2 - \frac{\varepsilon L_{\text{co}} T_c}{2(d_{g1} + y_0 + w_y)^2} V_a^2 + \frac{\varepsilon L_{\text{co}} T_c}{2(d_{g2} - y_0 - w_y)^2} V_a^2 \right], \quad (11)$$

where N_g is the number of gap-variant combs and y_0 is the initial misalignment along the y axis. The system dynamics under F_{eg} can be described as

$$m\ddot{w}_y + c\dot{w}_y + k_y w_y = F_y + F_{\text{eg}}, \quad (12)$$

where m , c , and k_y are the mass, damping, and stiffness of the swallow structure, respectively, and \dot{w}_y and \ddot{w}_y are the

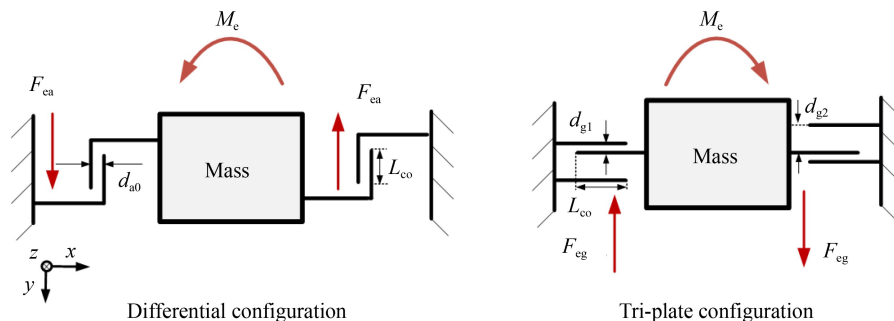


Fig. 6 Comb configuration utilized for area-variant and gap-variant devices.

first and second order derivative of w_y . The swallow structure is initially deformed under the normal electrostatic force F_{eg} . The pulling deformation can be calculated as

$$w_y = \frac{F_{eg}}{k_y}. \quad (13)$$

In the quasistatic measurement under a constant loading speed, Eq. (12) can be rewritten in terms of its derivative with respect to w_y :

$$k_y = N_g \left[\frac{\varepsilon L_{co} T_c}{(d_{g1} - y_0 - w_y)^3} V_a^2 + \frac{\varepsilon L_{co} T_c}{(d_{g2} + y_0 + w_y)^3} V_a^2 + \frac{\varepsilon L_{co} T_c}{(d_{g1} + y_0 + w_y)^3} V_a^2 + \frac{\varepsilon L_{co} T_c}{(d_{g2} - y_0 - w_y)^3} V_a^2 \right]. \quad (14)$$

The electrostatic force F_{eg} increases as the voltage bias V_a increases, and the movable structure is balanced at a new position with a larger w_y . For a critical voltage over V_{api} , the derivative of F_{eg} with respect to w_y could be larger than the stiffness k_y , and the movable plate approaches and finally contacts the fixed plate. V_{api} can be calculated as follows by substituting Eqs. (11) and (14) into Eq. (13) and neglecting the terms containing d_{g2} based on the Shenjing formula [39]:

$$V_{api} = \sqrt{\frac{k_y [3(y_0 + w_y)^2 - d_{g1}^2]^3}{2N_g \varepsilon L_{co} T_c d_{g1} [3(y_0 + w_y)^2 + d_{g1}^2]}}, \quad (15)$$

which is largely dependent on the displacement w_y and the stiffness ratio $r = \frac{k_y}{N_g}$. Figure 7(a) illustrates the relationship between the calculated V_{api} and w_y under different r values. In this calculation, y_0 is 0.001 μm ; the overlapped length L_{co} and T_c are 375 and 50 μm , respectively; air gap d_{g1} is 3 μm ; structure stiffness k_y is 22.75 N/m; and comb quantity N_g is 330. For a zero

displacement w_y , where no loading forces are applied, the initial V_{api} presents an increment from 1.66 to 3.33 V as r increases from 0.034 to 0.136 N/m. However, the force sensitivity deteriorates for a large k_y and small N_g . The pull-in voltage V_{api} decreases continuously from 2.35 to 1.03 V as structure displacement w_y increases to 1 μm at an r of 0.068. Therefore, the voltage bias should be set less than the minimum V_{api} throughout the structure movement.

The measured force $k_y(y_0 + w_y)$ is the sum of the loading force F_y and the electrostatic force F_{eg} . The measurement error from the electrostatic force E_{eg} can be calculated as

$$E_{eg} = \frac{F_{eg}}{k_y(y_0 + w_y) - F_{eg}}. \quad (16)$$

The relationship between E_{eg} and w_y is illustrated in Fig. 7(b), where stiffness ratio r is 0.068 and V_a changes from 0.20 to 1.00 V. The calculation results demonstrate that V_a can considerably affect measurement accuracy. For a large V_a of 1 V, E_{eg} is 21.92% in the initial state and reaches 29.42% as w_y increases to 1 μm . E_{eg} decreases below 3.77% and 0.23% during a 1 μm deformation for the small V_a values of 0.40 and 0.10 V, respectively. Traditional capacitance-voltage converters require a high V_a of over 1 V for higher sensitivity, which is no longer suitable for ultralow force sensing. A portable ASIC readout with a bias scaling circuit is proposed to attenuate this problem. The portable ASIC readout is discussed in the subsequent sections, wherein the voltage bias V_a can be scaled down below 0.10 V, and the electrostatic pulling interferences are thus well controlled.

3.2 Electrostatic rotation

The two opposite electrostatic forces in differential configurations can generate a planar electrostatic moment

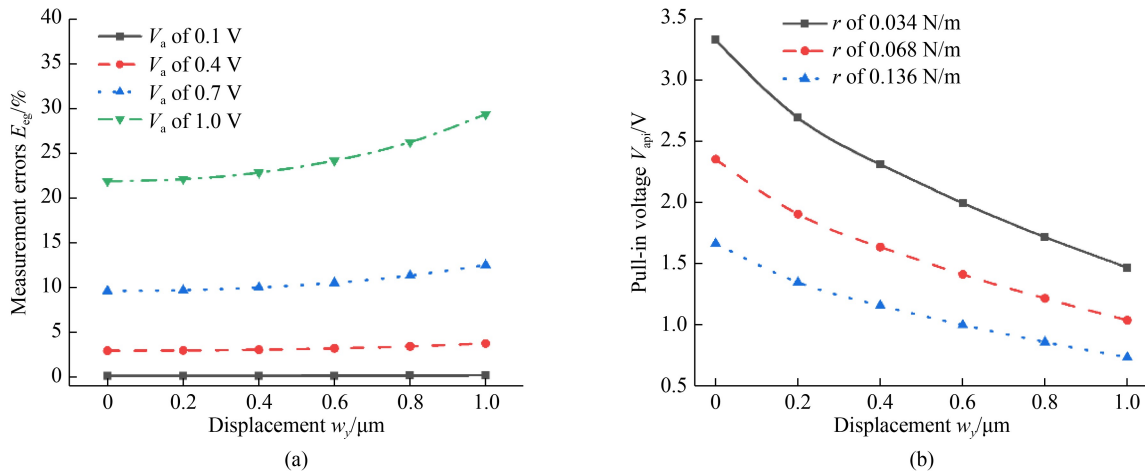


Fig. 7 Electrostatic pulling of the gap-variant capacitive combs: (a) relationship between the calculated V_{api} and displacement w_y under different stiffness ratio r and (b) relationship between the measurement error E_{eg} and displacement w_y under different voltage biases V_a .

M_e , which can easily rotate the swallow structure because of the low stiffness along the y axis, as shown in Fig. 7. In traditional differential arrangements, the rotation can be attenuated by increasing the structure stiffness or reducing the dimension and quantity of integrated combs but at the cost of force sensitivity. An asymmetric comb array distribution strategy is proposed in this work, where six feathered movable comb arrays are integrated along *Line_1*, *Line_2*, and *Line_3* inside both sides of the swallow structure. The corresponding fixed comb arrays were placed on the outside frame and two internal islands, as shown in Fig. 8. The negative sensing arrays C_{N1} , C_{N2} , and C_{N3} lie asymmetrically with respect to the structure center and constitute three differential pairs with the positive sensing arrays C_{P1} , C_{P2} , and C_{P3} . The resulting rotation moment M_e of negative or positive arrays can be calculated as

$$\begin{aligned} M_e = & F_e \left(\frac{1}{2} W_{\text{body}} + L_c - \frac{1}{2} L_{\text{co}} \right) \\ & + F_e \left(\frac{1}{2} W_{\text{body}} + W_{\text{is}} + 3L_c - \frac{3}{2} L_{\text{co}} \right) \\ & - F_e \left(\frac{1}{2} W_{\text{body}} + W_{\text{is}} + W_{\text{wing}} + 5L_c - \frac{5}{2} L_{\text{co}} \right), \end{aligned} \quad (17)$$

where W_{body} , W_{wing} , and W_{is} are the width of the swallow body, wing, and the internal island region, respectively, L_c is the length of the combs, and F_e is the general pulling electrostatic force in each comb array. The coupling rotation can be eliminated if the swallow body width follows the relationship,

$$W_{\text{body}} = 2W_{\text{wing}} + 2L_c - L_{\text{co}}. \quad (18)$$

The electrostatic coupling interferences can be eliminated by the following connection scheme: The

comb pads of the negative arrays C_{N1} , C_{N2} , and C_{N3} are connected in parallel to the common pad PAD_N , and the comb pads of the positive arrays C_{P1} , C_{P2} , and C_{P3} are connected to PAD_P , which share the same voltage bias with the excitation pad PAD_{EXC} in the movable structure. Four complementary comb arrays, namely, C_{C1} , C_{C2} , C_{C3} , and C_{C4} , have been integrated at the corners of the swallow structure to investigate the decoupling performance. Specifically, electrostatic pulling deformation can be measured with the differential output between the sum of the front comb arrays ($C_{C1} + C_{C2}$) and back arrays ($C_{C3} + C_{C4}$). Electrostatic rotation can be measured by utilizing the differential output of the two cater-cornered arrays, ($C_{C1} + C_{C3}$) and ($C_{C2} + C_{C4}$), as discussed in the next sections in detail.

4 Sensor preparation

4.1 Sensor fabrication

The proposed swallow capacitive sensor was fabricated using a four-inch silicon-on-insulator (SOI) wafer. The detailed three-mask fabrication process was reported in our previous works [25,26]. Figure 9 illustrates the microscopic observation of the fabricated gap-variant and area-variant sensors. The small geometric deviations that resulted from internal strain and manufacturing accuracy were observed and calibrated. Specifically, the area-variant sensor had air gaps of 3.33 and 14.73 μm for the asymmetric tri-plate configuration; the air gaps of the area-variant comb and complementary combs were 3.23 and 2.91 μm , respectively; and no comb stitching was observed. The beak probe had a step profile, and the width and length of its end effector were 2.46 and

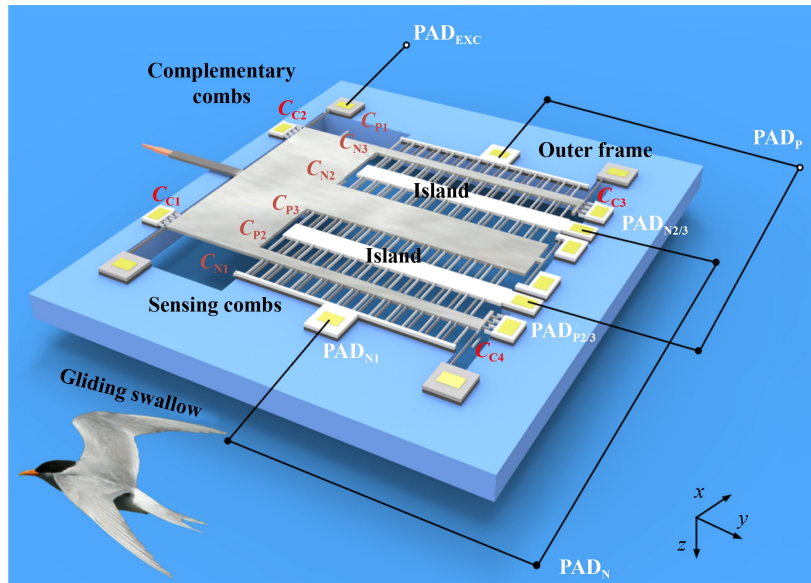


Fig. 8 Schematic of the proposed swallow structure.

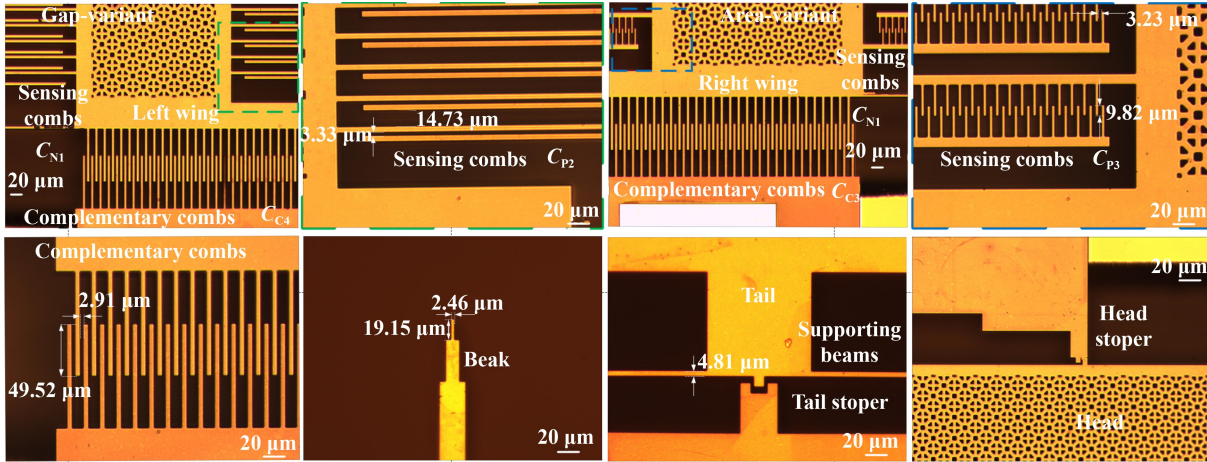


Fig. 9 Optical pictures of the fabricated gap-variant and area-variant type sensors.

19.15 μm , respectively. The movable swallow structure floated through the supporting beams with a measured width of 4.81 μm . Several stoppers were placed in the tail and head regions to limit excessive loading and protect the device.

4.2 Sensor readouts

The fabricated sensor was then packaged on a customized print circuit board (PCB), where a 24-bit ASIC chip (AD7746, Analog Devices) with a resolution of 4 aF and a measurement range of ± 21 pF was connected with the sensor combs for converting capacitance change into digital output. The positive and negative arrays were connected to the chip input pads C_{in+} and C_{in-} , respectively, which had the same voltage potential during operation. The AC excitation voltages, V_{EXCA} and V_{EXCB} , of the AD7746 chip were inverted, and their range was from -1.6 to $+1.6$ V, which probably resulted in electrostatic pull-in and produced substantial measurement error E_{eg} for gap-variant devices. Therefore, a bias-scaling circuit was proposed and integrated inside the

PCB, as shown in Fig. 10. The excitation voltage bias can be scaled into V_{EXC} with a scaling factor R of $\frac{R_1 + R_2}{R_1 - R_2}$, where parallel-connected R_1 and R_2 are the scaling resistors. Two frequency decoupling capacitors C_{d1} and C_{d2} were connected to the power supply electrode V_{cc} of the amplifier (AD8515, Analog Devices) for frequency decoupling. For area-variant devices, electrostatic pulling forces were constant and canceled out through differential configuration; thus, the movable comb pad was directly applied with a V_{EXCA} of ± 1.60 V.

5 Decoupling experiments

The four complementary comb arrays were first calibrated using a robotic microscopy system. On the basis of the calibrated differential output of these arrays and the proposed novel measurement readout, the electrostatic operation instability was measured, indicating that the electrostatic pulling and rotation interferences of the fabricated sensors were largely

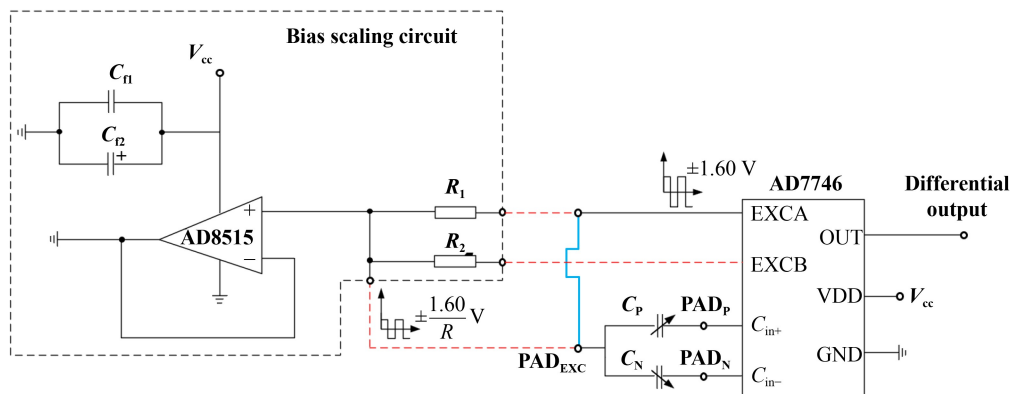


Fig. 10 Application-specific integrated circuit readouts integrated with a bias scaling circuit for the fabricated sensors of both types. The red and blue lines indicate the connection of area-variant and gap-variant sensors.

suppressed. Then, the mechanical decoupling experiments were conducted. Compared with the existing devices, the mechanical crosstalk was eliminated further, and a much higher sensitivity was obtained in this work. The detailed experimental results are discussed in the subsequent sections.

5.1 Electrostatic decoupling experiments

5.1.1 Complementary comb calibration

The sensing ability of four complementary comb arrays was calibrated before the electrostatic pulling experiments using a laboratory-built robotic microscopy system, as shown in Fig. 11. The packaged sensor was mounted on the manipulation stage through a 3D-printed polymethyl methacrylate (PMMA) connector. The manipulation stage incorporated a planar drive motor (P611.2S, PI) with a high positioning resolution of 0.2 nm and a vertical drive motor (XP-611.Z100S, XMT) with a positioning resolution of 1 nm. The targeted objects can be placed in the specimen stage, where a vertical drive motor (P611.ZS, PI) with a high vertical accuracy of 0.2 nm was integrated. This system also comprised an orthographic microscope module, which contains multiple objective lenses and a charge coupled device (CCD) camera (CS895CU, Thorlabs). The optical observation was automatically sampled and restored with the graphical user interface (GUI) inside the on-site computer, and the two moving stages could also be manipulated through the integrated closed-loop controller.

Before the experiment, the heights of the sensor probe and glass cube were alternately aligned into the focal plane. The sensor probe was orientated and adjusted to be perpendicular to the cube-side surface. The manipulation stage was used to move the sensor probe to approach the glass cube until an amplitude jump appeared on the recorded capacitive signal with a sampling rate of 9.1 Hz,

which indicated that the sensor probe had fully contacted the cube. The manipulation stage implemented step movements with a size Δd of 200 nm and held on the same position for the resting nine sampling moments. The front complementary sensing comb arrays, C_{C1} and C_{C2} , were in parallel connection with the connection pads PAD_{C1} and PAD_{C2} , which were then connected to the pad C_{in+} of the AD7746 chip and constituted a differential output with the connection pads PAD_{C3} and PAD_{C4} of the parallel-connected arrays C_{C3} and C_{C4} . The capacitive signals were measured for a total movement of 3 μm , and five repetitions were conducted to eliminate systematic errors, as shown in Fig. 12. The differential output $[(C_{C1} + C_{C2}) - (C_{C3} + C_{C4})]$ of both types exhibited identical responses. The average capacitive sensitivity S_c of five repeats was 23.405 fF/ μm for the gap-variant sensor and 23.253 fF/ μm for the area-variant sensor. The change in capacitance also showed a linear change during the whole movement range, and the average linearity was larger than 0.9999 for both devices. The electrostatic pulling deformation of the swallow sensor can be accurately measured by the differential output $[(C_{C1} + C_{C2}) - (C_{C3} + C_{C4})]$.

5.1.2 Electrostatic pulling experiments

The electrostatic pulling behavior of the area-variant type sensor was first studied. The four complementary comb arrays were differentially connected to the AD7746 chip, and the movable structure pad PAD_{EXC} was biased with the original excitation voltage V_{EXCA} of ± 1.60 V. A step DC voltage bias V_{dc} was separately applied to the positive pads i.e., PAD_{P1} , PAD_{P2} , and PAD_{P3} , and the negative pads, i.e., PAD_{N1} , PAD_{N2} , and PAD_{N3} , to evaluate the electrostatic pulling force of positive and negative arrays, as shown in Fig. 13. The efficient bias V_a across the comb arrays should be a combination of the DC and AC voltage bias. The swallow structure was pulled at a static position

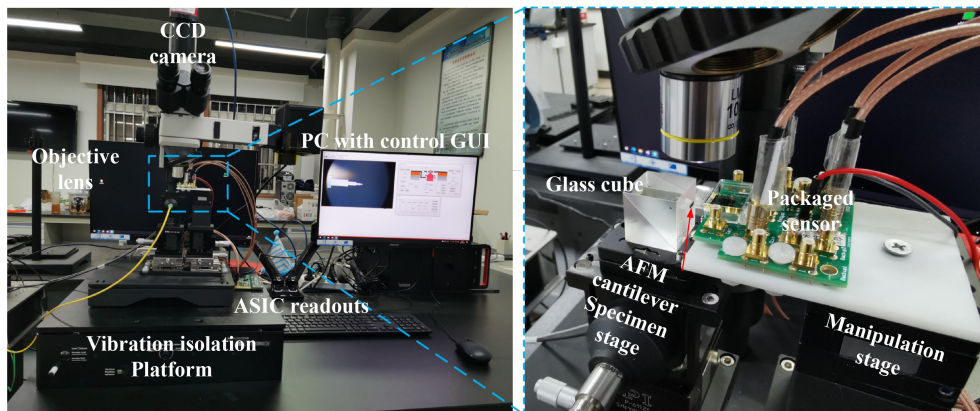


Fig. 11 Experimental setups of the built robotic microscopy system. AFM: atomic force microscope, ASIC: application-specific integrated circuit, CCD: charge coupled device, GUI: graphical user interface.

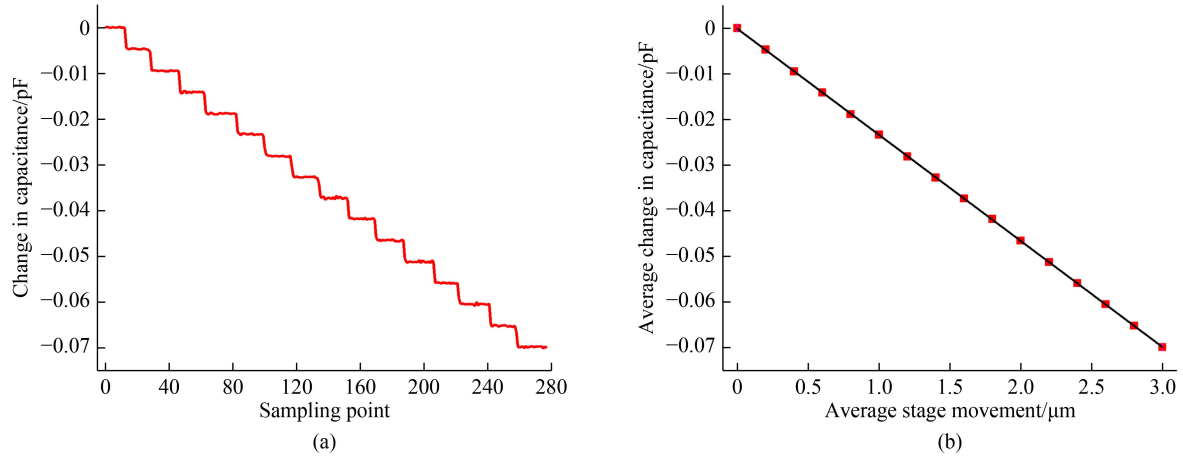


Fig. 12 Differential capacitive signal of complementary comb arrays under step movements: change in capacitance of $[(C_{C1} + C_{C2}) - (C_{C3} + C_{C4})]$ (a) for a movement with a step size of 200 nm and (b) during a total movement of 3 μm .

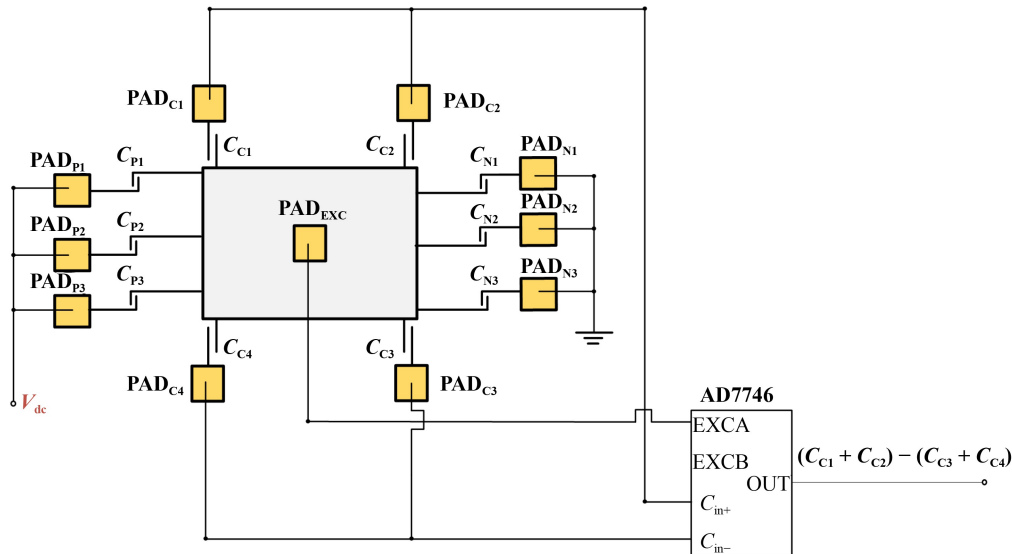


Fig. 13 Interconnection schematic for electrostatic pulling experiments of the area-variant sensor.

by the DC bias V_{dc} and then oscillated around this point because of the AC bias. However, the electrostatic force of the area-variant sensor was relatively small for the voltage bias of 1.60 V, and the DC bias became dominant as V_{dc} increased above 6.00 V. Therefore, the oscillation resulting from AC pulling is negligible for that moment. Figure 14(a) illustrates the change in capacitance of $[(C_{C1} + C_{C2}) - (C_{C3} + C_{C4})]$ as V_{dc} increased above 15.00 V. The capacitive output changed to 79.883 and 78.787 fF for the positive and positive arrays, respectively. In consideration of the capacitive sensitivity of the complementary comb arrays, the efficient pulling deformation values were 3.435 and 3.388 μm . The change in capacitance resulting from the electrostatic forces in the two array groups performed linear responses with the square of the applied voltage. This result indicated that the swallow structure was only involved in pulling translation instead of rotation. The pulling

deformation sensitivity values were 0.351 and 0.344 fF/V² for the positive and negative arrays, respectively.

The DC voltage bias V_{dc} was simultaneously applied to the positive pads, i.e., PAD_{P1}, PAD_{P2}, and PAD_{P3}, and the negative pads, i.e., PAD_{N1}, PAD_{N2}, and PAD_{N3}, to simulate the actual working condition. The electrostatic forces of the two array groups were canceled out by the differential configuration, as shown in Fig. 14(b). The capacitive signal rarely changed but performed small-scaled oscillation around the initial position because of the AC components. The maximum change in capacitance, $[(C_{C1} + C_{C2}) - (C_{C3} + C_{C4})]$, was 0.460 fF as V_{dc} increased above 15.00 V, and the largest pulling deformation was about 19.782 nm. The maximum voltage bias across the comb arrays was 1.60 V during sensor operation, and the corresponding electrostatic pulling deformation should be less than 0.770 nm considering the obtained pulling deformation sensitivity, which is less than 0.008% for the

sensor measurement range of 10 μm . However, this pulling deformation derived from fabrication asymmetry remained constant during sensor operation and can be directly compensated in the readouts.

Similarly, the positive and negative pads were simultaneously biased with the V_{dc} to study the pull-in behavior of the gap-variant device. However, the movable structure pad, PAD_{EXC} , was connected to the bias scaling circuit, where the excitation voltage V_{EXCA} was reduced to ± 0.36 V to lower the AC oscillation instability, as shown in Fig. 15. V_{dc} was gradually increased to avoid structure instability in the damped system. The movable combs snapped to the fixed ones once V_{dc} reached the pull-in voltage V_{api} , which was reflected by a capacitive jump in the differential output of $[(C_{C1} + C_{C2}) - (C_{C3} + C_{C4})]$. In the initial state, V_{api} was measured as 3.248 V

because of the geometric deviation y_0 . The sensor was then deformed with a step size of 200 nm under the robotic microscope. Figure 16(a) shows the measured V_{api} at different deformation positions. V_{api} decreased to 1.720 V when the sensor deformation reached 1.0 μm . The stiffness of the fabricated sensor was calibrated as 25.38 N/m, in accordance with the procedures in our previous works [25,26]. With the extracted parameters illustrated in Table 2, the theoretical curve from Eq. (15) presents a close estimation of the measured V_{api} . The measurement error E_{eg} can also be estimated on the basis of Eq. (16), as shown in Fig. 16(b). For the voltage bias V_a of ± 0.36 V, the maximum E_{eg} was less than 1.118% during the 1.0 μm deformation. Given that the measurement error E_{eg} had a small increase of 0.152 with respect to its initial state, E_{eg} can be easily compensated

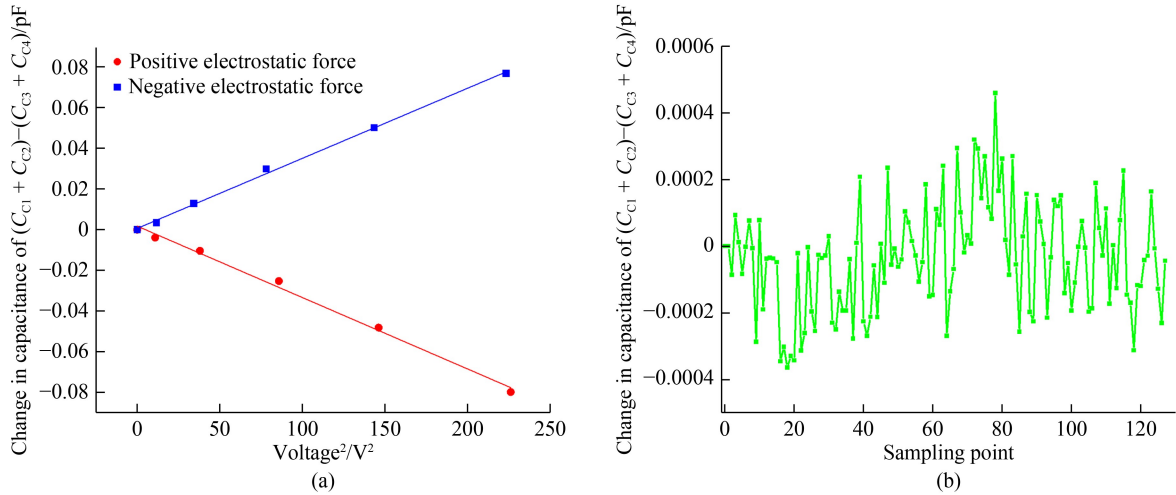


Fig. 14 Differential capacitive signal of complementary comb arrays under voltage bias: change in capacitance of $[(C_{C1} + C_{C2}) - (C_{C3} + C_{C4})]$ for (a) voltage separately biased at the positive and negative arrays and (b) voltage simultaneously biased at the positive and negative arrays.

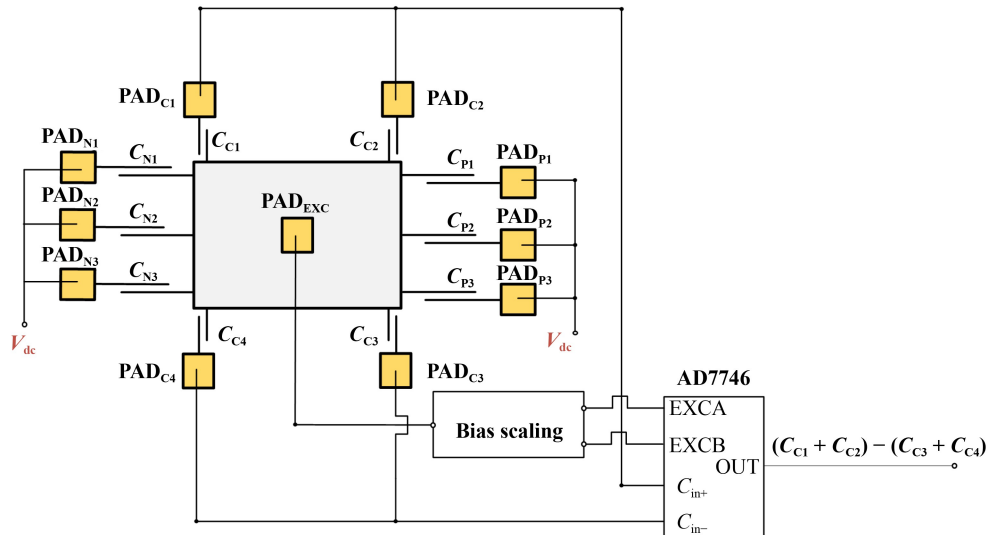


Fig. 15 Interconnection schematic for electrostatic pull-in experiments of the gap-variant sensor.

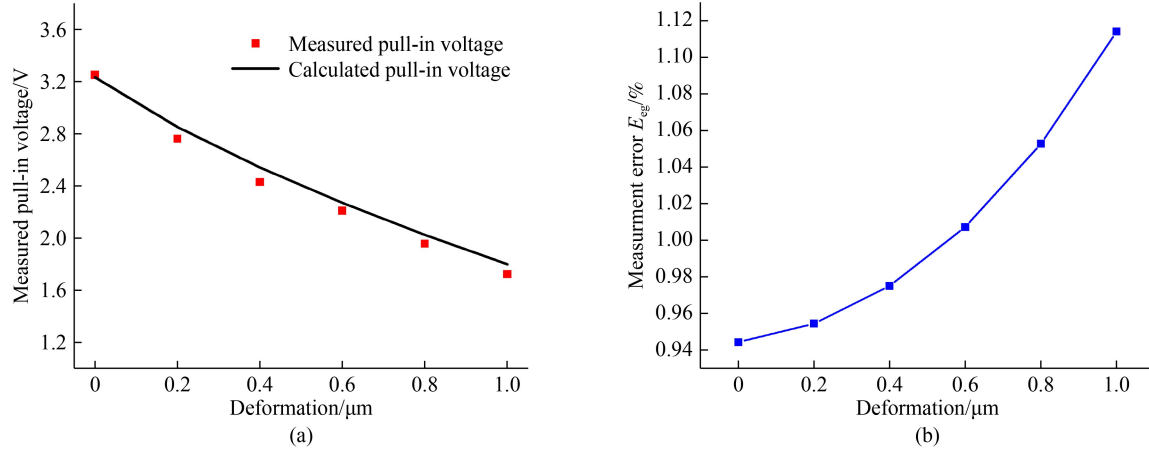


Fig. 16 Pull-in behavior of gap-variant sensor: (a) pull-in voltage V_{api} under different deformation and (b) measurement error E_{eg} under different deformation.

Table 2 Extracted parameters of the proposed gap-variant sensor

Parameter	Value
Efficient air gap of the combs, d_{g1}	3.90 μm
Initial misalignment, y_0	0.15 μm
Overlapped length of the combs, L_{co}	375 μm
Thickness of the combs, T_c	50 μm
Number of the combs, N_g	330
Stiffness along the y axis, k_y	25.38 N/m

in the subsequent readout circuits. Electrostatic pulling interferences of the proposed gap-variant sensor were also well controlled.

5.1.3 Electrostatic rotation experiments

Once a certain voltage bias is applied, the electrostatic moment can rotate the movable structure, which remains

constant for the area-variant device. For the gap-variant device, the electrostatic moment increases continuously during structure movement because electrostatic force is a function of structure position. Hence, the area-variant device was utilized to illustrate the rotation decoupling effectiveness of the proposed bionic design. The complementary comb arrays C_{C1} and C_{C3} showed opposite deformation with the cater-cornered arrays C_{C2} and C_{C4} , which were differentially connected to the readouts for rotation measurement. We first examined the self-decoupling performance of positive and negative comb arrays, wherein a DC voltage bias V_{dc} was separately applied to the positive and negative pad the positive pads, i.e., PAD_{P1} , PAD_{P2} , and PAD_{P3} , or the negative pads, i.e., PAD_{N1} , PAD_{N2} , and PAD_{N3} , as shown in Fig. 17. The differential output $[(C_{C1} + C_{C3}) - (C_{C2} + C_{C4})]$ remained because of the geometrical imperfections resulting from fabrication errors, but the change in capacitance from the

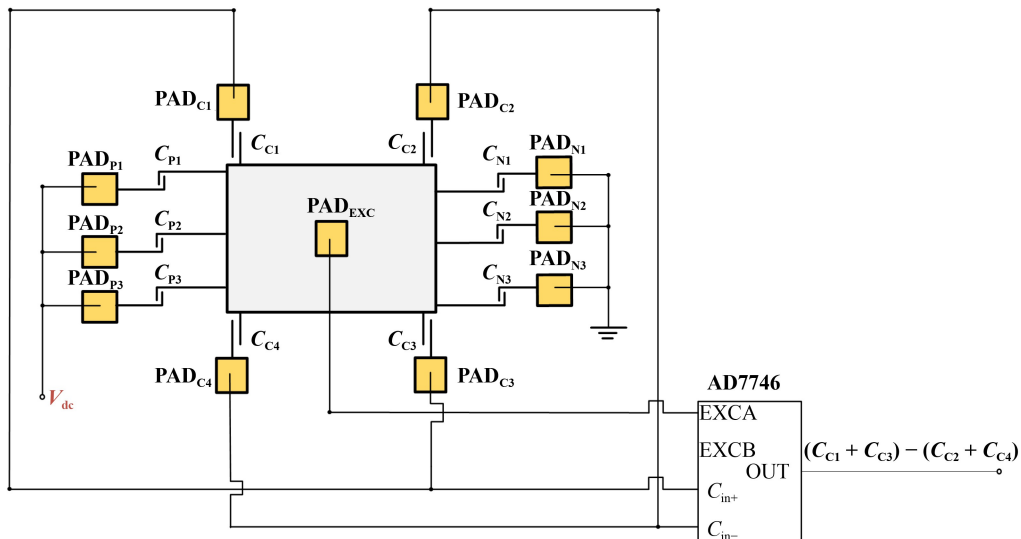


Fig. 17 Interconnection schematic for electrostatic rotation experiments of the area-variant sensor.

positive and negative electrostatic moments were less than 1.281 and 0.521 fF, respectively, even for a V_{dc} larger than 15.00 V, as shown in Fig. 18(a). The rotation deformation sensitivity values were 0.002 and 0.005 fF/V² for the positive and negative arrays, respectively.

V_{dc} was then simultaneously applied to the positive pads, i.e., PAD_{P1}, PAD_{P2}, and PAD_{P3}, and negative pads, i.e., PAD_{N1}, PAD_{N2}, and PAD_{N3}, to simulate the actual working condition. The change in capacitance oscillated around 0.552 fF when V_{dc} reached 15.00 V, as shown in Fig. 18(b). Assuming that $[(C_{C1} + C_{C3}) - (C_{C2} + C_{C4})]$ has the same capacitive sensitivity as $[(C_{C1} + C_{C2}) - (C_{C3} + C_{C4})]$, the rotation deformation was 23.739 nm, and the rotation angle was $(4.115 \times 10^{-5})^\circ$. Given the derived rotation deformation sensitivity, the rotation interferences for a normal bias of 1.60 V in sensor operation should be

less than $(5.694 \times 10^{-7})^\circ$ and 0.330 nm. When the sensor is loaded under a 1 μ N lateral force, the rotation deformation was less than 0.751% of the structure movement with a value of 43.939 nm. The gap-variant sensor has the same comb distribution with the area-variant type; therefore, the electrostatic rotation can be canceled out among the three positive or negative comb arrays.

The outside positive and negative arrays C_{P1} and C_{N1} were biased with DC voltage bias V_{dc} , constituting a traditional differential configuration for comparison experiments, as shown in Fig. 19. The differential output $[(C_{C1} + C_{C3}) - (C_{C2} + C_{C4})]$ increased linearly as V_{dc} increased and reached 6.560 fF at the V_{dc} of 15.00 V, as shown in Fig. 20. The efficient change in capacitance was 19.68 fF for the sensor integrating the same comb

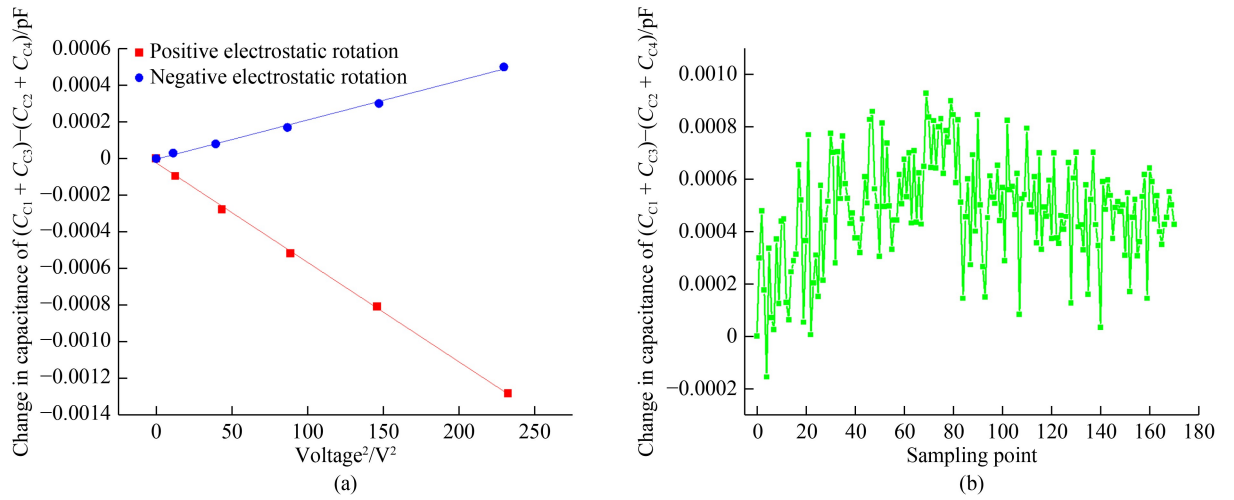


Fig. 18 Electrostatic rotation behavior of area-variant sensor: change in capacitance of $[(C_{C1} + C_{C3}) - (C_{C2} + C_{C4})]$ for (a) voltage separately biased at the positive and negative arrays and (b) voltage simultaneously biased at the positive and negative arrays.

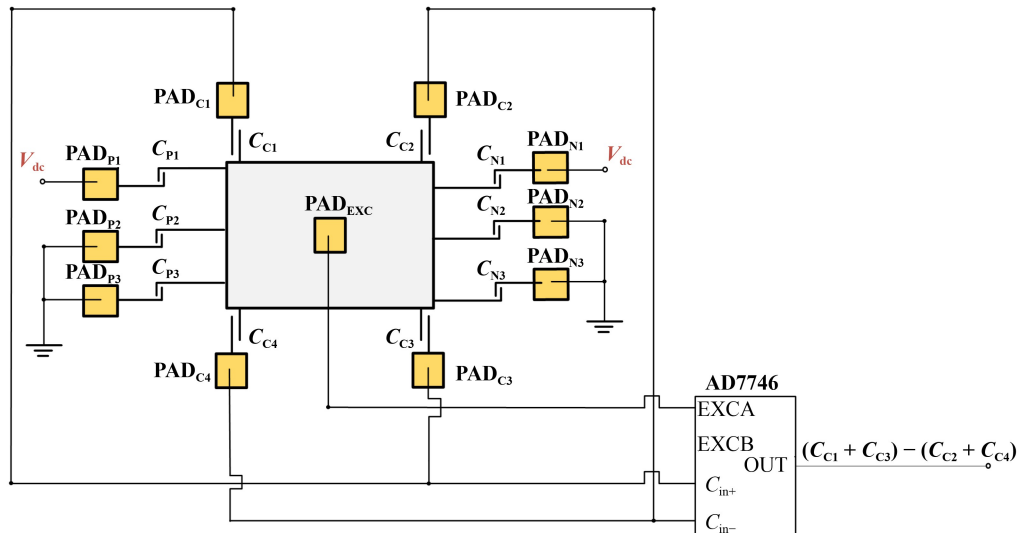


Fig. 19 Interconnection schematic for electrostatic rotation experiments of the traditional differential configuration.

quantity, the rotation deformation was 846.342 nm, and the rotation angle can reach $(1.467 \times 10^{-3})^\circ$, which was 35 times larger than that of the proposed sensor under the same bias.

5.2 Mechanical decoupling experiments

The fabricated sensor was applied with the forces along three axes to verify the mechanical decoupling performance, as shown in Fig. 21. A rigid glass tube was first assembled on the specimen stage, and loading force F_y was applied to the sensor probe once the sensor was manipulated to compress the cube side surface following the same procedures. Notably, a mirror reflection inside the cube showed high symmetry with the sensor probe about the cube side surface, indicating the interaction force was solely from the y axis, as shown in Fig. 21(a). Given the large stiffness difference between the sensor and rigid glass. The glass cube was barely deformed, and the interaction force F_y was fully applied to the sensor probe with a constant increment of $k_y \Delta d$, as shown in Fig. 22. The red curve in Fig. 22(a) illustrates the

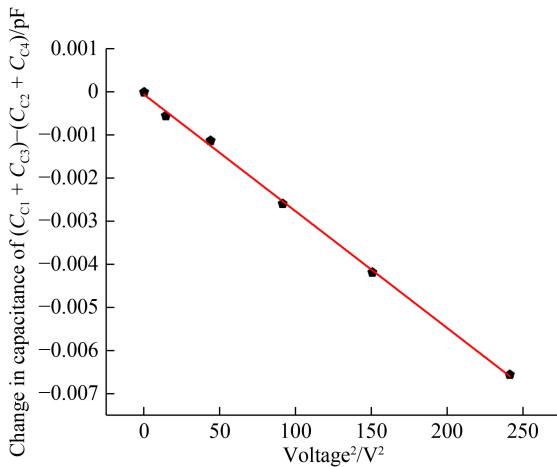


Fig. 20 Change in capacitance of $[(C_{C1} + C_{C3}) - (C_{C2} + C_{C4})]$ for voltage only biased at the outside positive and negative arrays.

capacitive change of the gap-variant sensor for a step movement of $1 \mu\text{m}$, where the applied voltage bias was scaled down to $\pm 0.36 \text{ V}$. The red curve in Fig. 22(c) illustrates the capacitive change of the gap-variant sensor for a step movement of $2 \mu\text{m}$, but the voltage bias V_{EXC} applied to the area-variant devices remained at $\pm 0.36 \text{ V}$. The capacitive signal presented a step profile during the step movement of the manipulation stage. However, we also found some small fluctuations in each step plane of the recorded capacitive signal and stage position, which resulted from the slippery interaction and environmental oscillation. Figures 22(b) and 22(d) illustrate the relationship between the average change in capacitance and corresponding average stage position. The capacitive signal of the area-variant device exhibited an increment of 2.926 pF for $2 \mu\text{m}$ deformation, and the capacitive change of the gap-variant device reached 7.114 pF for $1 \mu\text{m}$ deformation. The capacitive sensitivity under force along y axis was calculated as the slope of the fitting line, which was $7.078 \text{ pF}/\mu\text{m}$ with a linearity of 0.9996 for the gap-variant device and $1.473 \text{ pF}/\mu\text{m}$ with a linearity of 0.9998 for the area-variant device. To the best of our knowledge, the fabricated sensor exhibited the highest sensitivity among the current devices.

The fabricated sensor was then applied with the forces along the x and z axes to verify the mechanical decoupling performance. Compared with the force loading experiments along the y axis, the mounted sensor was moved to compress an atomic force microscope (AFM) cantilever (SNL-10, Bruker) at its base section. The AFM base had a sharper indenter and a clearer optical boundary than the previously adopted glass cube. Thus, the interaction process between the sensor probe and targeted AFM cantilever base was easily monitored under microscopic observation, as shown in Figs. 21(b) and 21(c). Moreover, the AFM cantilever base had a thickness larger than $6000 \mu\text{m}$, guaranteeing its high resistivity against compression deformation along the y axis and bending deformation along the z axis. Once the sensor probe contacts the base, the stage movement can also be fully converted into loading forces on the sensor probe.

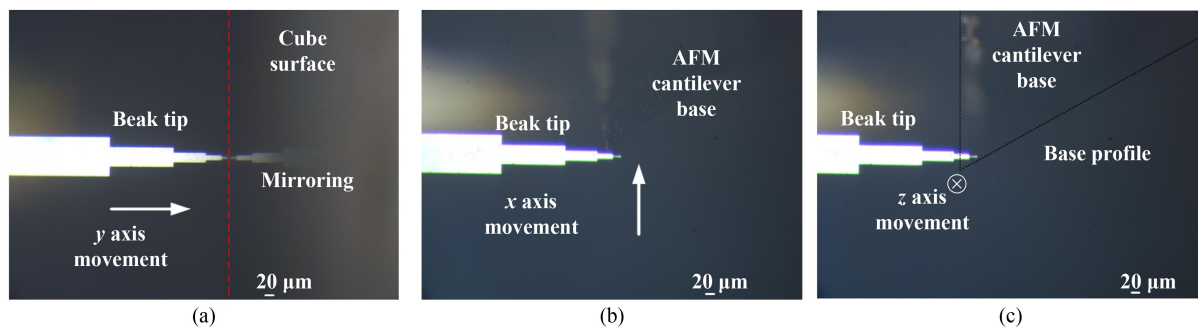


Fig. 21 Experimental procedures of mechanical loading along three axes: (a) y axis loading with the glass cube, (b) loading along the x axis with the AFM cantilever base, and (c) loading along z axis with the AFM cantilever base. AFM: atomic force microscope.

In accordance with similar alignment procedures, the sensor probe was manipulated to pull the AFM cantilever base along the x and z axes with a step size Δd of 200 nm. Figure 23 illustrates the capacitive change of the gap-

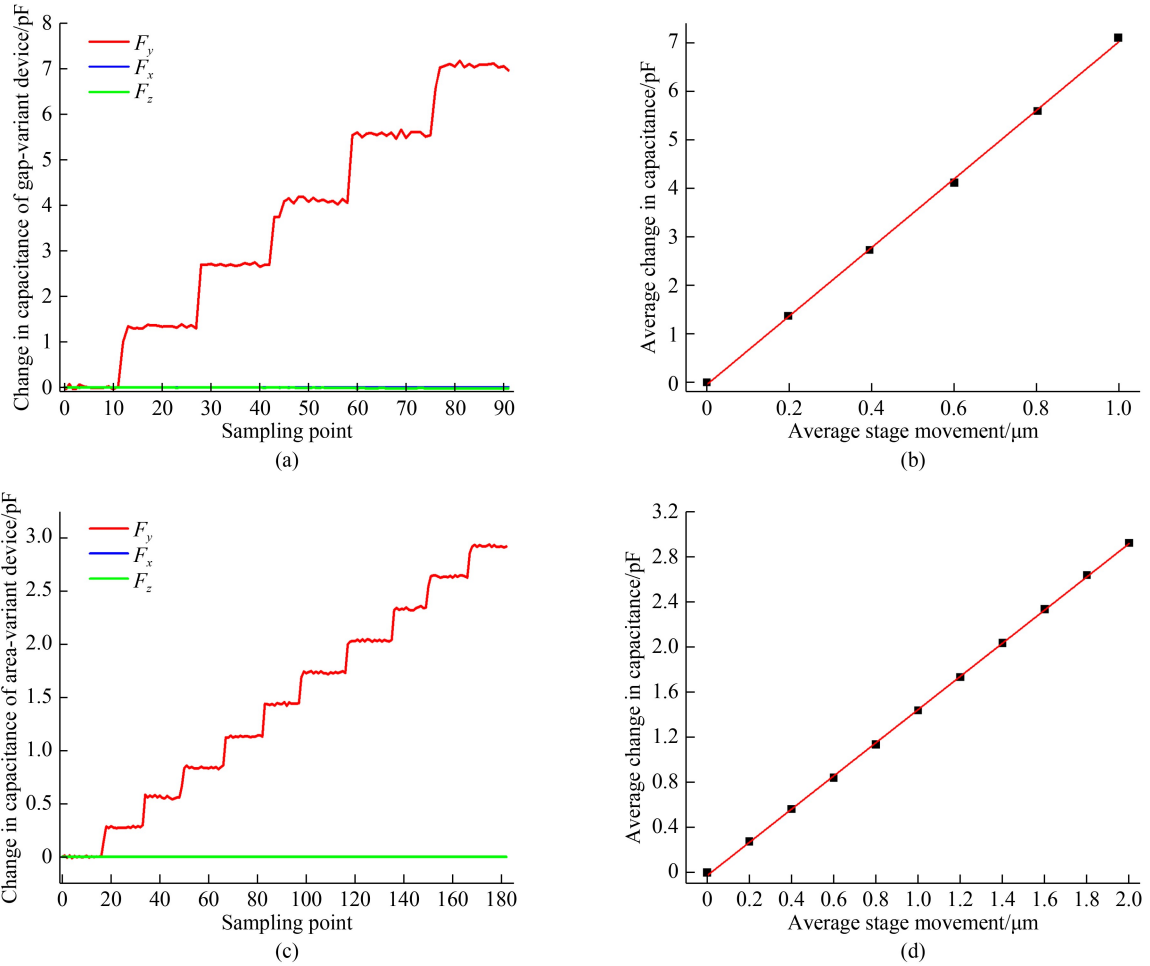


Fig. 22 Capacitive signal under force along y axis F_y : (a) change in capacitance of the gap-variant sensor for a step movement of 1 μm , (b) average change in capacitance of the gap-variant sensor during step movement, (c) change in capacitance of the area-variant sensor for a step movement of 1 μm , and (d) average change in capacitance of the area-variant sensor during step movement.

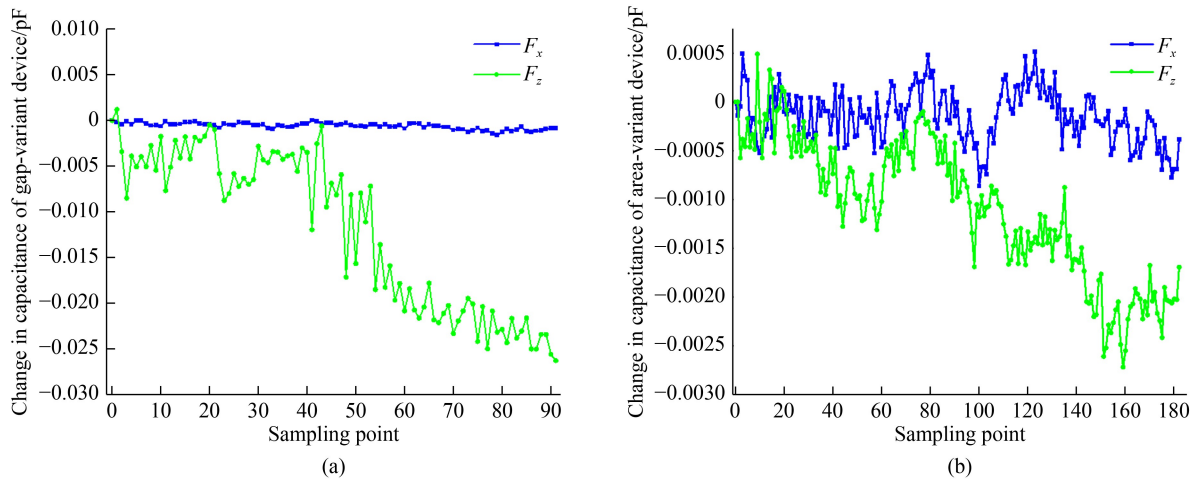


Fig. 23 Capacitive signal under force along the x axis F_x and z axis F_z : (a) change in capacitance of the gap-variant sensor for a step movement of 1 μm and (b) change in capacitance of the area-variant sensor for a step movement of 2 μm .

variant and area-variant sensors under forces F_x and F_z . Similar to the theoretical analysis, the swallow sensor was rarely deflected under F_x , as reflected by the blue curves in both figures. The capacitive change exhibited small fluctuations of 0.840 fF for the gap-variant device under 1 μm lateral interferences and 0.383 fF for the area-variant device under 2 μm lateral interferences, which were only 0.012% and 0.013% for those devices under the same loadings along the y axis, respectively. The capacitive signal presented relatively larger responses for vertical interferences. Specifically, the change in capacitance increased to 26.257 fF for the gap-variant device under 1 μm interferences and 1.694 fF for the area-variant device under 2 μm interferences. Compared with the change in capacitance under y axis loadings, the vertical crosstalk took less than 0.369% and 0.058% of the sensor outputs. The bionic swallow structure design can simultaneously guarantee high capacitive sensitivity and mechanical decoupling performance.

5.3 Performance comparison and analysis

Based on the proposed bionic method, the fabricated sensors improved its coupling immunity against electrostatic and mechanical interferences, as shown in Table 3 [23,24,30,31]. The electrostatic pulling was less than 0.009% for the proposed gap-variant sensor, which was identical to the area-variant capacitive devices in current studies. However, rare attention has been paid to the electrostatic interferences in gap-variant devices. In this work, the electrostatic pulling behavior was comprehensively analyzed using the proposed gap-variant sensor, whose measurement error was 1.118% and can be compensated in the following readouts. The electrostatic rotation was calibrated for the first time, the proposed sensors presented 35 times improvement compared with the traditional differential capacitive sensors, and the resulting measurement error was less than 0.751%. The proposed method also improved mechanical decoupling performance. Specifically, the planar and vertical crosstalk was 0.012% and 0.058% for the proposed area-variant sensor, which were much lower than the area-

variant device with the corresponding values of 8.116% and 1.926%, respectively [31]. The proposed gap-variant sensor exhibited a low planar crosstalk of 0.012% and vertical crosstalk was 0.369%, which was about ninth of the vertical crosstalk of the gap-variant sensor with a value of 3.226% [30]. Given the excellent decoupling ability, the proposed sensors possessed overwhelming sensing performance in comparison with the existing devices. The capacitive sensitivity was 1.473 pF/ μm for the proposed area-variant sensor, which was 6.08 times for the reported area-variant device with a value of 0.242 pF/ μm and 2.48 times for the device with the value of 0.595 pF/ μm . As for the gap-variant device, the capacitive sensitivity of the proposed sensor was 7.078 pF/ μm , which was 7.59 times for the device with the value of 0.933 pF/ μm and 2.74 times for the device with the value of 2.581 pF/ μm . High linearity was simultaneously maintained, which was 0.9998 and 0.9996 for the proposed sensor of both types. Therefore, the so-called trade-off problem between the coupling resistance and sensing performance was delicately solved with the proposed bionic method.

6 Conclusions

In this work, a bionic approach was developed for the mechanical and electrical decoupling of capacitive sensors. The influence of mechanical and electrostatic interferences can be largely eliminated with the bionic swallow structure and feather comb distribution strategy. The electrostatic pulling of the area-variant sensor was less than 0.770 nm, and the measurement error was less than 0.009% for the area-variant sensor and 1.118% for the gap-variant sensor. A high resistance against electrostatic rotation was also achieved for the proposed sensor, and the rotation interferences should be less than 0.330 nm and $(5.694 \times 10^{-7})^\circ$, which were 35 times smaller than those of the traditional differential sensor. The measurement error from electrostatic rotation was less than 0.751%. The fabricated sensor showed high capacitive sensitivity of 7.078 and 1.473 pF/ μm along the

Table 3 Performance comparison with existing devices [23,24,30,31]

Previous works	Capacitive sensitivity (pF· μm^{-1})	Linearity	Electrostatic pulling*/%	Electrostatic rotation*/%	Mechanical crosstalk/%
Area-variant [23]	0.242	0.9997	N	Y	Na
Gap-variant [24]	2.581	0.9800	Y	Y	Na
Gap-variant [30]	0.001	Na	Y	Y	3.226 (vertical)
Area-variant [31]	0.595	0.9700	N	Y	8.116 (planar); 1.926 (vertical)
Bionic area-variant (this work)	1.473	0.9998	0.009	0.751	0.013 (planar); 0.058 (vertical)
Bionic gap-variant (this work)	7.078	0.9996	1.118	0.751	0.012 (planar); 0.369 (vertical)

Notes. * "Y" indicates that the sensor suffers from the electrostatic coupling effect. "N" indicates that the sensor is insusceptible from the electrostatic coupling effect.

sensing direction for gap-variant and area-variant devices, respectively, and the mechanical crosstalk produced less than 0.369% and 0.058% of the sensor outputs for the gap-variant and area-variant devices, respectively, indicating the effectiveness of this approach for high-resolution measurement in biomedical applications.

Nomenclature

Abbreviations

AFM	Atomic force microscope
ASIC	Application-specific integrated circuit
CCD	Charge coupled device
GUI	Graphical user interface
MEMS	Micro-electro-mechanical system
PCB	Print circuit board
PMMA	Polymethyl methacrylate
SOI	Silicon-on-insulator

Variables

c	Damping of the swallow structure
C	Overlapped area of the comb capacitor
$C_{C1}, C_{C2}, C_{C3}, C_{C4}$	Complementary comb arrays
C_{d1}, C_{d2}	Frequency decoupling capacitors of the bias-scaling circuit
C_{in+}, C_{in-}	Inputs of the ASIC chip
C_{N1}, C_{N2}, C_{N3}	Negative sensing arrays
C_{P1}, C_{P2}, C_{P3}	Positive sensing arrays
d	Gap of the combs
d_{a0}	Initial gap of the area-variant combs
d_{g1}, d_{g2}	Air gap of the gap-variant combs
Δd	Step size of the manipulation stage movements
D_1, D_2, D_3	Distances between six supporting beams and the structure center
E	Young's modulus of the movable structure
E_{eg}	Measurement error from the electrostatic force of gap-variant device
$F_{0yi}, F_{0zi} (i = 1, 2, \dots, 6)$	Reaction forces along the y and z axis at the fixed end of supporting beams, respectively
F_c	General pulling electrostatic force of comb arrays
F_{ea}, F_{eg}	Pulling electrostatic forces of the area- and gap-variant comb arrays, respectively
F_x, F_y, F_z	Loading forces along the x , y , and z axis at the beak tip, respectively
F'_z	Equivalent force along the z axis at the structure center

I_y, I_z	Moment inertia around the y and z axis of the beam lateral section, respectively
k_y	Stiffness of the swallow structure
L_b	Length of the supporting beam
L_{body}, L_{beak}	Lengths of the swallow body region and beak probe, respectively
L_c	Length of the comb plate
L_{co}	Overlapped length of the combs
$L_{head}, L_{tail}, L_{wing}$	Lengths of the swallow head region, tail region, and wing region, respectively
L_{off}	Offset distance between the structure center and front frame of the head region
$Line_1$	Sampling line along the swallow body
$Line_2$	Sampling line along the inside frames of the swallow wing
$Line_3$	Sampling line along the outside frames of the swallow wing
m	Mass of the swallow structure
M_{0y}, M_{0z}	Reaction moments around the y and z axis at the fixed end of supporting beams, respectively
M_c	Planar electrostatic moment of comb arrays
M_x	Moment around the x axis derived from F_z
N_{as}, N_g	Numbers of the area- and gap-variant combs, respectively
$PAD_{Ci} (i = 1, 2, \dots, 4)$	Comb pads of the complementary sensing arrays
$PAD_{Ni} (i = 1, 2, 3)$	Comb pads of the negative sensing arrays
$PAD_{Pi} (i = 1, 2, 3)$	Comb pads of the positive sensing arrays
PAD_{EXC}	Excitation pad
r	Stiffness ratio
R	Scaling factor of the bias-scaling circuit
R_1, R_2	Scaling resistors of the bias-scaling circuit
S_c	Capacitive sensitivity of the complementary comb arrays
T_b	Thickness of the supporting beam
T_c	Thickness of the combs
V_a	Applied voltage bias between the combs
V_{api}	Critical voltage applied to the gap-variant combs
V_{cc}	Power supply of the ASIC chip
V_{dc}	DC bias applied to the combs
V_{EXC}	Scaled excitation voltages of the ASIC chip
V_{EXCA}, V_{EXCB}	Excitation voltages of the ASIC chip
w_E	Elastic deformation along the z axis derived from F_z
w_{Fz}	Translation bending deformation along the z axis derived from F_z
w_{Mz}	Rotation bending deformation along the z axis derived from M_x

w_x	Bending deformation along the x axis
w_y	Bending deformation along the y axis
\dot{w}_y	First order derivative of w_y
\ddot{w}_y	Second order derivative of w_y
w_z	Bending deformation along the z axis
W_b	Width of the supporting beams
$W_{\text{body}}, W_{\text{is}}, W_{\text{wing}}$	Widths of the swallow body region, island region, and wing region, respectively
y_0	Initial misalignment of the asymmetrical gap-variant combs
ε	Dielectric permittivity in air
δ_y	Bending angle along the y axis

Acknowledgements This work was supported in part by the National Natural Science Foundation of China (Grant Nos. 52105589 and U1909221), in part by the China Postdoctoral Science Foundation (Grant No. 2021M692590), in part by the Fundamental Research Funds for the Central Universities, China (Grant No. xzy012021009), in part by the State Key Laboratory of Robotics and Systems (HIT), China (Grant No. SKLRS2021KF17), and in part by the Beijing Advanced Innovation Center for Intelligent Robots and Systems, China (Grant No. 2019IRS08).

Conflict of Interest The authors declare that they have no conflict of interest.

References

- Shakoor A, Wang B, Fan L, Kong L C, Gao W D, Sun J Y, Man K, Li G, Sun D. Automated optical tweezers manipulation to transfer mitochondria from fetal to adult MSCs to improve antiaging gene expressions. *Small*, 2021, 17(38): e2103086
- Bohineust A, Garcia Z, Corre B, Lemaître F, Bousso P. Optogenetic manipulation of calcium signals in single T cells *in vivo*. *Nature Communications*, 2020, 11(1): 1143
- Pan L M, Liu J N, Shi J L. Cancer cell nucleus-targeting nanocomposites for advanced tumor therapeutics. *Chemical Society Reviews*, 2018, 47(18): 6930–6946
- Felekis D, Vogler H, Mecja G, Muntwyler S, Nestorova A, Huang T Y, Sakar M S, Grossniklaus U, Nelson B J. Real-time automated characterization of 3D morphology and mechanics of developing plant cells. *The International Journal of Robotics Research*, 2015, 34(8): 1136–1146
- Krenger R, Burri J T, Lehnert T, Nelson B J, Gijs M A M. Force microscopy of the *Caenorhabditis elegans* embryonic eggshell. *Microsystems & Nanoengineering*, 2020, 6(1): 29
- Läubli N F, Burri J T, Marquard J, Vogler H, Mosca G, Vertti-Quintero N, Shamsudhin N, DeMello A, Grossniklaus U, Ahmed D, Nelson B J. 3D mechanical characterization of single cells and small organisms using acoustic manipulation and force microscopy. *Nature Communications*, 2021, 12(1): 2583
- Madsen L S, Waleed M, Casacio C A, Terrasson A, Stilgoe A B, Taylor M A, Bowen W P. Ultrafast viscosity measurement with ballistic optical tweezers. *Nature Photonics*, 2021, 15(5): 386–392
- Dai C S, Zhang Z R, Lu Y C, Shan G Q, Wang X, Zhao Q L, Sun Y. Robotic orientation control of deformable cells. In: *Proceedings of the 2019 International Conference on Robotics and Automation (ICRA)*. Montreal: IEEE, 2019, 8980–8985
- Xie Y, Sun D, Tse H Y G, Liu C, Cheng S H. Force sensing and manipulation strategy in robot-assisted microinjection on zebrafish embryos. *IEEE/ASME Transactions on Mechatronics*, 2011, 16(6): 1002–1010
- Wei Y Z, Xu Q S. A survey of force-assisted robotic cell microinjection technologies. *IEEE Transactions on Automation Science and Engineering*, 2019, 16(2): 931–945
- Koo B, Ferreira P M. An active MEMS probe for fine position and force measurements. *Precision Engineering*, 2014, 38(4): 738–748
- Grech D, Tarazona A, De Leon M T, Kiang K S, Zekonyte J, Wood R J K, Chong H M H. A quasi-concertina force-displacement MEMS probe for measuring biomechanical properties. *Sensors and Actuators A: Physical*, 2018, 275: 67–74
- Wei Y Z, Xu Q S. Design and testing of a new force-sensing cell microinjector based on small-stiffness compliant mechanism. *IEEE/ASME Transactions on Mechatronics*, 2021, 26(2): 818–829
- Curry E J, Ke K, Chorsi M T, Wrobel K S, Miller A N, Patel A, Kim I, Feng J L, Yue L X, Wu Q, Kuo C L, Lo K W H, Laurencin C T, Ilies H, Purohit P K, Nguyen T D. Biodegradable piezoelectric force sensor. *Proceedings of the National Academy of Sciences*, 2018, 115(5): 909–914
- Xie Y, Zhou Y L, Lin Y Z, Wang L Y, Xi W M. Development of a microforce sensor and its array platform for robotic cell microinjection force measurement. *Sensors*, 2016, 16(4): 483
- Dostanić M, Windt L M, Stein J M, Van Meer B J, Bellin M, Orlova V, Mastrangeli M, Mummery C L, Sarro P M. A miniaturized EHT platform for accurate measurements of tissue contractile properties. *Journal of Microelectromechanical Systems*, 2020, 29(5): 881–887
- Lai W J, Cao L, Liu J J, Chuan Tjin S, Phee S J. A three-axial force sensor based on fiber Bragg gratings for surgical robots. *IEEE/ASME Transactions on Mechatronics*, 2022, 27(2): 777–789
- Gao W D, Jia C, Jiang Z D, Zhou X Y, Zhao L B, Sun D. The design and analysis of a novel micro force sensor based on depletion type movable gate field effect transistor. *Journal of Microelectromechanical Systems*, 2019, 28(2): 298–310
- Gao W D, Qiao Z X, Han X G, Wang X Z, Shakoor A, Liu C L, Lu D J, Yang P, Zhao L B, Wang Y L, Wang J H, Jiang Z D, Sun D. A MEMS micro force sensor based on a laterally movable gate field-effect transistor (LMGFET) with a novel decoupling sandwich structure. *Engineering*, 2023, 21: 61–74
- Xu Q S. *Micromachines for Biological Micromanipulation*. Cham: Springer, 2018
- Zhang Y R, Jen Y H, Mo C T, Chen Y W, Al-Romaihy M, Martincic E, Lo C Y. Realization of multistage detection sensitivity and dynamic range in capacitive tactile sensors. *IEEE Sensors Journal*, 2020, 20(17): 9724–9732
- Shakoor A, Gao W D, Zhao L B, Jiang Z D, Sun D. Advanced tools and methods for single-cell surgery. *Microsystems & Nanoengineering*, 2022, 8(1): 47
- Zhang H C, Wei X Y, Ding Y Y, Jiang Z D, Ren J. A low noise capacitive MEMS accelerometer with anti-spring structure.

- Sensors and Actuators A: Physical, 2019, 296: 79–86
24. Li R, Mohammed Z, Rasras M, Elfadel I A M, Choi D. Design, modelling and characterization of comb drive MEMS gap-changeable differential capacitive accelerometer. *Measurement*, 2021, 169: 108377
 25. Gao W D, Liu C L, Han X G, Zhao L B, Lin Q J, Jiang Z D, Sun D. A high-resolution MEMS capacitive force sensor with bionic swallow comb arrays for ultralow multiphysics measurement. *IEEE Transactions on Industrial Electronics*, 2023, 70(7): 7467–7477
 26. Gao W D, Liu C L, Liu T, Zhao L B, Wang C Y, Shakoor A, Luo T, Jing W X, Yang P, Lin Q J, He Y Q, Dong T, Jiang Z D, Sun D. An area-variant type MEMS capacitive sensor based on a novel bionic swallow structure for high sensitive nano-indentation measurement. *Measurement*, 2022, 200: 111634
 27. Gao W D, Shakoor A, Xie M Y, Chen S X, Guan Z Y, Zhao L B, Jiang Z D, Sun D. Precise automated intracellular delivery using a robotic cell microscope system with three-dimensional image reconstruction information. *IEEE/ASME Transactions on Mechatronics*, 2020, 25(6): 2870–2881
 28. Gao W D, Shakoor A, Zhao L B, Jiang Z D, Sun D. 3-D image reconstruction of biological organelles with a robot-aided microscopy system for intracellular surgery. *IEEE Robotics and Automation Letters*, 2019, 4(2): 231–238
 29. Gao W D, Zhao L B, Jiang Z D, Sun D. Advanced biological imaging for intracellular micromanipulation: methods and applications. *Applied Sciences*, 2020, 10(20): 7308
 30. Felekis D, Muntwyler S, Vogler H, Beyeler F, Grossniklaus U, Nelson B J. Quantifying growth mechanics of living, growing plant cells *in situ* using microrobotics. *Micro & Nano Letters*, 2011, 6(5): 311–316
 31. Li Z, Gao S, Brand U, Hiller K, Wolff H. A MEMS nanoindenter with an integrated AFM cantilever gripper for nanomechanical characterization of compliant materials. *Nanotechnology*, 2020, 31(30): 305502
 32. Monsalve J M, Melnikov A, Kaiser B, Schuffenhauer D, Stolz M, Ehrig L, Schenk H A G, Conrad H, Schenk H. Large-signal equivalent-circuit model of asymmetric electrostatic transducers. *IEEE/ASME Transactions on Mechatronics*, 2022, 27(5): 2612–2622
 33. Zhang H C, Wei X Y, Gao Y, Cretu E. Analytical study and thermal compensation for capacitive MEMS accelerometer with anti-spring structure. *Journal of Microelectromechanical Systems*, 2020, 29(5): 1389–1400
 34. Poletkin K V. Static pull-in behavior of hybrid levitation microactuators: simulation, modeling, and experimental study. *IEEE/ASME Transactions on Mechatronics*, 2021, 26(2): 753–764
 35. Ma Z P, Jin X J, Guo Y X, Zhang T F, Jin Y M, Zheng X D, Jin Z H. Pull-in dynamics of two MEMS parallel-plate structures for acceleration measurement. *IEEE Sensors Journal*, 2021, 21(16): 17686–17694
 36. Nastro A, Ferrari M, Ferrari V. Double-actuator position-feedback mechanism for adjustable sensitivity in electrostatic-capacitive MEMS force sensors. *Sensors and Actuators A: Physical*, 2020, 312: 112127
 37. Maroufi M, Alemansour H, Moheimani S O R. A high dynamic range closed-loop stiffness-adjustable MEMS force sensor. *Journal of Microelectromechanical Systems*, 2020, 29(3): 397–407
 38. Li C, Zhang D, Cheng G, Zhu Y. Microelectromechanical systems for nanomechanical testing: electrostatic actuation and capacitive sensing for high-strain-rate testing. *Experimental Mechanics*, 2020, 60(3): 329–343
 39. Fan S J. A new extracting formula and a new distinguishing means on the one variable cubic equation. *Natural Science Journal of Hainan Teachers College*, 1989, 2(2): 91–98 (in Chinese)